Int. J. Ind. Chem. 2026; 17(2): 79-104

International Journal of Industrial Chemistry (IJIC)

https://doi.org/10.57647/IJIC.2026.1702.08

Research Article

An Efficient, Solvent-Free Synthesis of Xanthene Derivatives Using Z-NTS@Cu as a Reusable and Eco-Friendly Nano-catalyst

Mohammad Reza Haghshenas [1], Seyed Mohammad Vahdat [1]*, Hasan Tahermansouri [1], Behrooz Maleki [2]

[1] *Department of Chemistry, Am.c. Islamic Azad University, Amol, Iran*

[2] *Department of Organic Chemistry, Faculty of Chemistry, University of Mazandaran, Babolsar, Iran*

***Corresponding author:** Sm.vahdat@iau.ac.ir

Article History:

Received:
27 February 2026

Revised:
30 March 2026

Accepted:
18 April 2026

Published in Issue:
30 June 2026

Abstract

In this study, a green and efficient one-pot multi-component protocol was developed for synthesizing a wide range of xanthene derivatives using (Z-NTS@Cu) as an eco-friendly and recyclable Nano-catalyst. The reactions proceeded under solvent-free conditions, providing excellent yields. The heterogeneous catalyst was prepared via stepwise surface modification of zeolite, which serves as a high-surface-area support with functionalizable active sites. The zeolite was first modified with 3-aminopropyl triethoxysilane (APTES) to introduce amino groups, followed by anchoring of cyanuric chloride (TCT) as a triazine linker, and subsequent immobilization of thiosemicarbazide. This functionalization created nitrogen and sulfur donor sites capable of stable copper coordination. Comprehensive characterization of the catalyst was performed using FT-IR, XRD, SEM, TEM, BET, TGA, EDX-EDS, and EDX mapping analyses, confirming successful functionalization and uniform copper distribution. The synergistic effect between the zeolite framework and the copper-thiosemicarbazide complex contributed to high catalytic activity and selectivity in multi-component reactions. The catalyst's heterogeneous nature allowed straightforward separation and reuse for up to six consecutive cycles without significant loss of efficiency. Importantly, the reactions proceeded under mild conditions, highlighting the catalyst's practicality and environmentally benign profile. Overall, the Z-NTS@Cu nanocatalyst represents a sustainable, reusable, and highly effective system for the green synthesis of xanthene derivatives, combining high performance, ease of recovery, and minimal environmental impact. Its design demonstrates how functionalized zeolite-supported copper complexes can advance eco-friendly organic synthesis while maintaining operational simplicity and excellent catalytic outcomes.

Keywords: Nanocatalyst, Zeolite, Green organic synthesis, Xanthene

Cite this article: Haghshenas M.R., Vahdat S.M., Tahermansouri H., Maleki B., An Efficient, Solvent-Free Synthesis of Xanthene Derivatives Using Z-NTS@Cu as a Reusable and Eco-Friendly Nano-catalyst. Int. J. Ind. Chem. 2026; 17(2): 79-104. https://doi.org/10.57647/IJIC.2026.1702.08

1. Introduction

As global awareness of the environmental impacts related to industrial activities increases, considerable efforts have been directed toward the development of eco-friendly sustainable approaches to chemical synthesis[1-3]. In this context, the development of green chemical systems that reduce energy consumption [4], limit the use of toxic

solvents and hazardous materials, while maintaining high efficiency and selectivity, has emerged as a central objective of sustainable chemistry [5–8]. Among the principal strategies in green chemistry, the use of recyclable heterogeneous catalysts plays a critical role in reducing environmental impacts and advancing cleaner industrial processes [9, 10]. Consequently, the development of green and sustainable catalytic systems [11, 12] for chemical synthesis has become a scientific imperative [13, 14]. Green and sustainable synthetic systems employ a range of support materials to achieve high catalytic efficiency while minimizing environmental impact [15, 16]. Among these, crystalline porous materials[17] include zeolites, ordered mesoporous silica, and metal organic frameworks (MOFs) [18, 19]. Although their common features endow these porous materials with many advantageous properties, their differences determine the advantages and disadvantages for particular applications, especially catalysis.

Zeolites, owing to their crystalline porous architecture and hydrated alumina-silicate frameworks, exhibit large internal and external surface areas [20] that can be readily modified through surface functionalization [21, 22]. Such functionalization is commonly accomplished through covalent attachment of organic or inorganic functional groups [23], including amines, thiols or halogenated moieties, thereby enabling the stable immobilization of catalytic species or metal ligands [24, 25]. Surface modification of zeolites not only increases the density and uniform dispersion of active sites but also enhances their thermal and chemical stability under multistep reaction conditions, effectively suppressing metal leaching and aggregation [26, 27]. Moreover, surface functionalization modulates the physicochemical properties of zeolites, including acidity, hydrophobicity, and pore confinement effects, which can directly influence catalytic activity, selectivity [28], and reaction kinetics [29, 30]. For example, the incorporation of acidic or basic functionalities can facilitate electron transfer processes and strengthen interactions between reactants and metal active sites. Consequently, functionalized zeolites are widely recognized as advanced supports for green and sustainable synthesis, playing a crucial role in enhancing the efficiency, selectivity, and long-term stability of heterogeneous catalysts [31, 32].

The aim of this project is to design, synthesize, and systematically evaluate the catalytic performance of the Nano-composite (Z-NTS@Cu). This catalyst operates as an efficient heterogeneous copper-based system owing to the synergistic interactions between the zeolite support and the immobilized Cu–thiosemicarbazide complex. The zeolite framework offers a high surface area, thermal stability, and accessible acidic sites, which promote substrate adsorption and enhance reaction rates. Functionalization with APTES facilitates the covalent attachment of cyanuric chloride [33], serving as a rigid Triazine linker that enables the stable immobilization of thiosemicarbazide ligands. The thiosemicarbazide moiety, featuring nitrogen and sulfur donor atoms, strongly coordinates copper ions [34], resulting in well-dispersed and stable Cu active centers on the support. These copper sites act as Lewis acidic and redox-active centers, facilitating the efficient activation of organic substrates, including alkynes, carbonyl compounds, and heteroatom-containing reactants. Accordingly, the catalyst demonstrates high activity across a range of organic transformations, such as C–N and C–S coupling reactions, multicomponent reactions, Michael-addition [35], and Knoevenagel-type [36, 37] processes. The heterogeneous nature of the catalyst enables facile separation from the reaction mixture and substantially minimizes copper leaching, ensuring excellent recyclability and long-term operational stability.

2. Experimental

2.1. Materials

All chemicals were purchased from Merck and Sigma-Aldrich and used without further purification.

2.2. Instruments

The physicochemical properties of the synthesized materials were investigated using several analytical techniques. Melting points were measured with an IA9100 electrothermal apparatus. Fourier-transform infrared (FT-IR) spectra were recorded on a Shimadzu IR-470 spectrophotometer. ^{1}H and ^{13}C nuclear magnetic resonance (NMR) spectra were recorded on a Bruker 400 MHz NMR spectrometer. Transmission electron microscopy (TEM) images were obtained using a Philips EM-208S microscope, and scanning electron microscopy (SEM) images were collected with a MIRA III-XMU instrument. X-ray diffraction (XRD) patterns were recorded using a Philips PW-1830 diffractometer. The specific surface area and textural properties were determined by Brunauer–Emmett–Teller (BET) analysis using nitrogen adsorption–desorption isotherms, and Thermogravimetric analysis (TGA) was performed on a Q600 instrument (TA Instruments).

2.3. Synthesis of Z-PrNH$_2$

Nano-zeolite (1.0 g) was dispersed in 30 mL of anhydrous toluene and refluxed for 25 min under a nitrogen atmosphere. Subsequently, 3 mL of 3-aminopropyltriethoxysilane (APTES) was added, and the reaction mixture was refluxed for 18 h. Upon completion of the reaction, the resulting solid was separated by filtration. After cooling to room temperature, the solid was

further collected by centrifugation. To remove unreacted APTES, the solid was subjected to Soxhlet extraction with 200 mL of ethanol for 24 h [38, 39].

2.4. Synthesis of Z-NT

1.0 g of the Nano-particles obtained in the preceding step was dispersed in 40 mL of anhydrous tetra-hydrofuran (THF). Subsequently, cyanuric chloride (TCT) (0.5 g) and Et_3N (0.3 g) were added to the suspension, and the reaction mixture was stirred at 0–5 °C. After completion of the reaction, the nanoparticles were isolated by centrifugation and washed repeatedly with THF [40].

2.5. Synthesis of Z-NTS

1.0g of Z-NT was dispersed in 30 mL of anhydrous tetrahydrofuran (THF). Subsequently, thiosemicarbazide (0.5 g) and Et_3N (0.3 g) were added to the reaction mixture at 0–5 °C, and the suspension was stirred for 12 h. The resulting nanoparticles were then separated using an external magnetic field and washed repeatedly with ethanol (EtOH) [41].

2.6. Synthesis of Z-NTS@CU

1.0 g of the Nano-catalyst Z-NTS was dispersed in 30 mL of ethanol (EtOH), after which $Cu(OAc)_2$ (0.91 g) was added. The reaction mixture was stirred at 70 °C for 18 h. Upon completion, the catalyst was recovered by centrifugation and washed repeaztedly with ethanol (Scheme 1).

2.7. General procedure for synthesis of xanthene derivatives

As shown in Scheme 2, a mixture of benzaldehydes (1 mmol), 1,3-cyclohexanedione (dimedone, 1 mmol), and 2-naphthol (β-naphthol, 1 mmol) was added to a reaction vessel containing the synthesized Z-NTS@CU catalyst (10 mg). The resulting mixture was stirred under solvent-free conditions at 70 °C, and the reaction progress was monitored by thin-layer chromatography (TLC). After completion, the reaction mixture was allowed to cool to room temperature, followed by the addition of ethyl acetate (10 mL). The catalyst was separated by centrifugation, and the supernatant was washed with water (10 mL). Finally, the crude product was purified by recrystallization from ethanol.

2.8. Optimization of reaction conditions

The reaction conditions for the synthesis of xanthene derivatives were optimized using a model three-component reaction of 2-hydroxybenzaldehyde, dimedone, and β-naphthol catalyzed by Z-NTS@CU. Important parameters, including solvent, amount of Nano-catalyst, reaction time, and temperature, were investigated to maximize catalytic efficiency. The effect of Z-NTS@CU nanocatalyst loading on reaction efficiency was examined by varying the catalyst amount while keeping all other reaction parameters constant.

Catalyst loadings of 5, 10, 15, and 20 mg were evaluated. As summarized in Table 1, increasing the catalyst amount from 5 to 10 mg resulted in a marked improvement in reaction efficiency. However, further increases beyond 10 mg did not lead to any noticeable enhancement, indicating that 10 mg is the optimal catalyst loading for this transformation.

Solvent screening revealed that nonpolar solvents afforded low yields and prolonged reaction times, while polar aprotic solvents showed moderate performance due to partial coordination to the Lewis acidic copper centers. Polar protic solvents significantly improved reaction outcomes; however, the highest yield and shortest reaction time were achieved under solvent-free conditions. Evaluation of reaction time demonstrated that product yield increased with time until complete conversion was reached, after which no further improvement was observed. Temperature optimization indicated that elevated temperatures enhanced reaction rate and yield up to an optimal point, beyond which no significant benefits were observed. Accordingly, the optimal conditions for xanthene synthesis were identified as solvent-free operation at 70 °C with a reaction time of 20-30 min (Table 2).

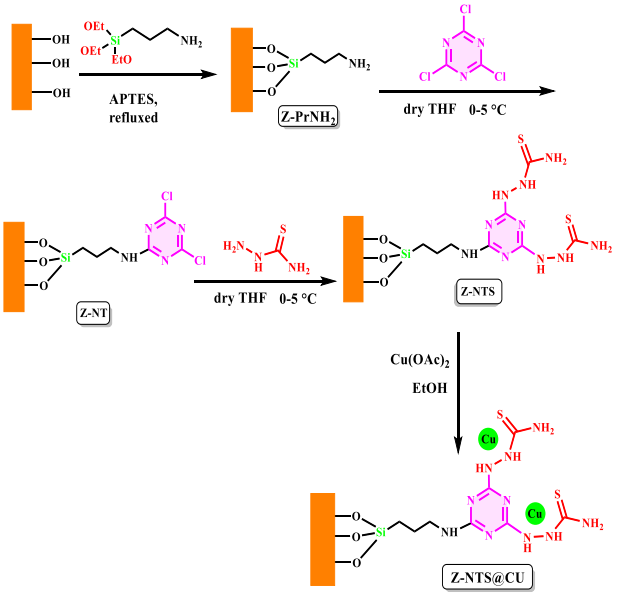

Scheme 1. Steps for Synthesis of Z-NTS@CU Nano-catalyst

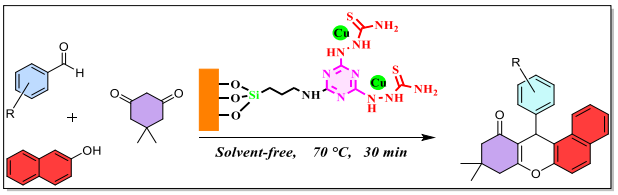

Scheme 2. synthesis of xanthene derivatives

10.57647/ijic.2026.1702.08

Table 1. Optimization of Z-NTS@CU Nano-catalyst amount (mg)

Entry	Catalyst amount (mg)	Efficiency (%)
1	5	80
2	10	98
3	15	98
4	20	98

3. Results and discussions

3.1. Characterization of Z-NTS@CU Nano-Catalyst

3.1.1. *Fourier transform infrared spectroscopy (FT-IR)*

The FT-IR spectrum of the parent zeolite displays characteristic absorption bands associated with the aluminosilicate framework and surface hydroxyl groups. A strong band at 1000–1100 cm^{-1} corresponds to the asymmetric stretching of Si–O–Si and Si–O–Al bonds, confirming the structural integrity of the zeolite, while a weaker band near 800 cm^{-1} is attributed to symmetric Si–O–Si stretching, typical of crystalline zeolites. Bands in the 500–600 cm^{-1} range are assigned to double-ring vibrations of the zeolite structural units. Functionalization with APTES introduces organic features, evidenced by a broad band at 3900–3600 cm^{-1} due to –OH stretching of surface silanols and adsorbed water, a shoulder at 3370–3180 cm^{-1} corresponding to N–H stretching of amino groups, and bands at 2990–2850 cm^{-1} assigned to $–CH_2–$ stretching of the propyl chain, confirming successful grafting of the organic moiety. The zeolite framework remains intact, as indicated by persistent strong bands at 1000–1200 cm^{-1}. Additional bands at 1500–1650 cm^{-1} correspond to C=N stretching of the triazine ring, and weak bands at 650–850 cm^{-1} are attributed to residual C–Cl stretching from cyanuric chloride. Further functionalization with thiosemicarbazide is confirmed by N–H stretching at 3100–3400 cm^{-1} and C=O/C=S stretching around 1630–1650 cm^{-1}, accompanied by a slight decrease in the broad –OH band (3700–3850 cm^{-1}) due to reaction with surface hydroxyls. C–H stretches of the propyl chain (2850–2950 cm^{-1}) and the characteristic zeolite framework bands (1000–1200 cm^{-1}) remain unchanged. Upon copper coordination, the characteristic vibrations of the zeolite and organic linkers are preserved, while slight shifts in N–H stretching (3200–3400 cm^{-1}) and N–H bending vibrations, as well as bands at 1500–1700 cm^{-1} corresponding to C=N (cyanuric chloride) and C=S (thiosemicarbazide) stretching, indicate Cu–N and Cu–S interactions. Minor residual C–Cl bands (650–850 cm^{-1}) are also observed, confirming the maintenance of functionalized features and successful copper immobilization (Fig. 1).

3.1.2. *X-ray diffraction (XRD) analysis*

The X-ray diffraction pattern of Z-NTS@CU exhibits the characteristic diffraction reflections of the zeolite framework at 2θ: 7° and 22°, 25°, indicating that the crystalline structure of the zeolite is well preserved following surface functionalization. In comparison with pristine zeolite, a noticeable reduction in peak intensity accompanied by slight peak broadening is observed, which can be attributed to successful grafting of organic moieties and a partial increase in amorphous character without inducing structural collapse. Furthermore, the presence of weak and broad diffraction peaks at 2θ: 35°, 43, 45° and 50° is assigned to copper species (Cu^0 or Cu_2O,CuO), implying their high dispersion and Nano-scale crystallite size on the zeolite surface, with no evidence of bulk copper phase formation (Fig.2).

3.1.3. *Thermo-gravimetric analysis (TGA)*

The TGA curves of Z-$PrNH_2$, Z-NTS, and Z-NTS@Cu are presented in Fig. 3 and provide valuable insights into the thermal stability of the materials as well as the amount of organic matter immobilized on the zeolite framework. For Z-$PrNH_2$, an initial weight loss of approximately 5–7% is observed in the temperature range of 30–150 °C, which can be attributed to the removal of physically adsorbed moisture and residual solvents. A subsequent gradual weight loss of about 12–15% occurs between 150 and 700 °C and is associated with the thermal decomposition of amino-propyl groups grafted onto the zeolite surface, indicating good stability of this surface modification. In comparison, Z-NTS exhibits a noticeably higher weight loss than Z-$PrNH_2$. The initial weight loss of around 6–8% below 150 °C corresponds to the elimination of adsorbed water. The main decomposition stage takes place in the temperature range of 200–500 °C, accounting for approximately 25–30% of the total weight, and is attributed to the degradation of organic moieties introduced through the attachment of cyanuric chloride and thiosemicarbazide to the zeolite structure. This multistep degradation behavior confirms the successful execution of the stepwise chemical functionalization. Among the samples, Z-NTS@Cu shows the highest weight loss, reflecting the increased loading of organic components and copper-containing complexes. An initial weight loss of about 5–6% below 150 °C is again associated with the removal of surface moisture. The most pronounced weight loss occurs between 300 and 400 °C, with a value of approximately 30–35%, which is assigned to the decomposition of organic ligands and copper coordination complexes. The total weight loss reaches approximately 40–45% at 700 °C, while the inorganic zeolite framework retains its thermal stability.

10.57647/ijic.2026.1702.08

Table 2. Optimization of the synthesis conditions of xanthene derivatives in the presence of the Z-NTS@CU Nano-catalyst

Entry	Solvent	Conditions	Time (min)	Catalyst amount (mg)	Yield (%)
1	Solvent-free	70 °C	30	10	98
2	H_2O	Reflux	45	10	78
3	EtOH	Reflux	30	10	90
4	EtOH:H_2O (1:1)	Reflux	35	10	88
5	MeOH	Reflux	40	10	82
6	CH_3CN	Reflux	50	10	70
7	CH_2Cl_2	Reflux	60	10	65
8	Toluene	Reflux	90	10	55
9	DMF	100 °C	60	10	68

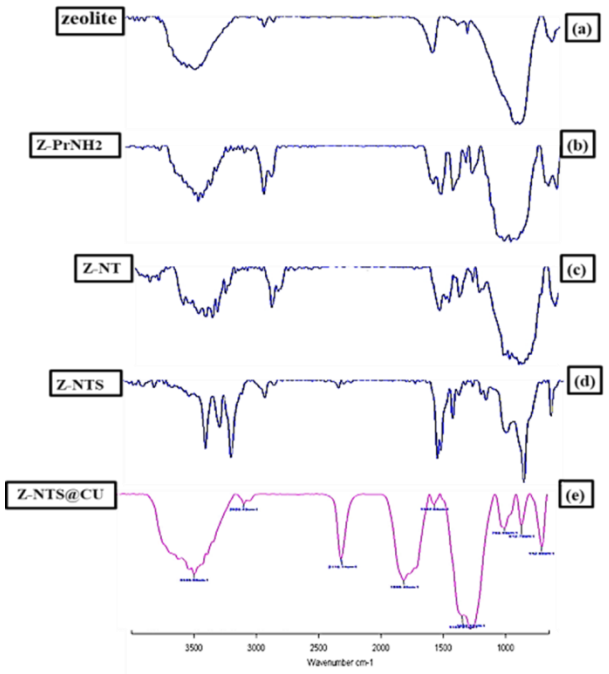

Figure 1. FT-IR spectrum of the synthetic steps of Z-NTS@CU Nano-catalyst

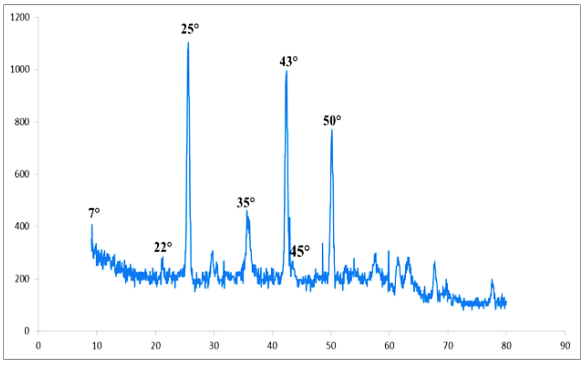

Figure 2. XRD analysis of Z-NTS@CU Nano-catalyst

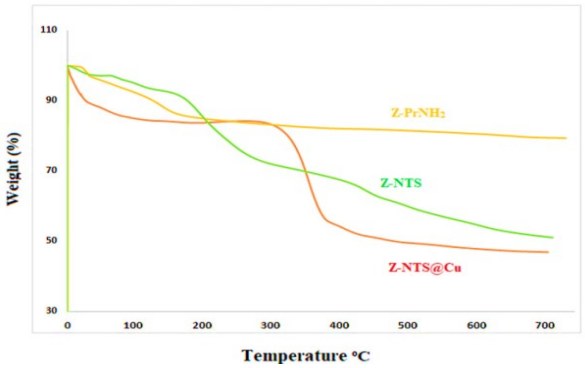

Figure 3. TGA curves of Z-NTS@CU Nano-catalyst

3.1.4. *Brunauer–Emmett–Teller (BET) analysis*

Nitrogen adsorption–desorption analysis indicates that stepwise surface modification of the zeolite and subsequent immobilization of copper species have a pronounced impact on the textural properties of the materials. The Z-$PrNH_2$ sample exhibits a BET specific surface area of 17.05 $m^2\ g^{-1}$, an average pore diameter of 20.3 nm, and a total pore volume of 0.09 $cm^3\ g^{-1}$ (Table 3), reflecting a predominantly mesoporous structure. Following chemical functionalization and copper loading, the specific surface area of Z-NTS@Cu decreases markedly to 6.19 $m^2\ g^{-1}$, accompanied by a reduction in pore diameter of 16.4 nm and pore volume of 0.03 $cm^3\ g^{-1}$ (Table 4). These changes can be attributed to the occupation and partial blockage of zeolite channels by grafted organic ligands and copper coordination complexes. The t-plot analysis further supports this trend. Z-$PrNH_2$ displays a total specific surface area of 10.63 $m^2\ g^{-1}$, with the dominant contribution arising from micropores (10.51 $m^2\ g^{-1}$), while the external surface area contributes negligibly (0.12 $m^2\ g^{-1}$). In contrast, Z-NTS@Cu shows a substantial decrease in both micropore surface area (2.42 $m^2\ g^{-1}$) and total specific surface area (2.62 $m^2\ g^{-1}$), providing clear evidence that a significant fraction of the micropores is filled by immobilized organic and metal species. Overall, these textural modifications confirm the successful formation of the Z-NTS@Cu nanocatalyst with well-defined and effectively confined active sites.

BET and t-plot analyses of Z-$PrNH_2$ and Z-NTS@Cu reveal the effects of sequential functionalization and Cu immobilization on porosity. The linear BET region (p/p_0 = 0.05–0.30) confirms the mesoporous nature of both materials. Z-NTS@Cu exhibits consistently lower nitrogen uptake compared to Z-$PrNH_2$, reflecting a significant reduction in accessible surface area due to pore

10.57647/ijic.2026.1702.08

occupation by grafted organic groups and coordinated Cu species. t-plot analysis further shows that Z-PrNH$_2$ maintains substantial micropore volume, whereas Z-NTS@Cu displays a reduced slope, indicating pronounced micropore filling and associated loss of surface area resulting from the immobilized organic framework and Cu complexes (Fig. 4).

3.1.5. *Transmission electron microscopy (TEM) analysis*

TEM analysis confirms successful stepwise surface functionalization and effective copper immobilization in the Z-NTS@CU composite. The zeolite framework remains structurally intact, with a uniformly distributed thin organic layer on the particle surfaces. Copper species are finely and homogeneously dispersed without aggregation, indicating strong coordination with the nitrogen- and sulfur-containing functional groups (Fig. 5).

3.1.6. *Field emission scanning electron microscopy (FE-SEM) analysis*

FE-SEM analysis of the Z-NTS@CU Nano-catalyst reveals systematic morphological evolution, confirming the successful functionalization of the zeolite surface. The pristine zeolite maintains its crystalline structure, while successive modifications increase surface roughness and heterogeneity. Copper species are uniformly dispersed on the surface without aggregation, indicating successful immobilization and preservation of the zeolite framework (Fig.6).

3.1.7. *Energy-dispersive X-ray analysis (EDX)*

EDX analysis of Z-NTS@CU confirms the successful stepwise functionalization of the zeolite and effective copper incorporation. The spectrum shows the characteristic elements of the zeolite framework, with Si (13.93 w%) and Al (6.99 w%) indicating that the structural integrity is maintained, while O (17.48 w%) originates from both the zeolite lattice and the grafted organic layers. The presence of C (21.96 w%) and N (4.45 w%) confirms the attachment of APTES, cyanuric chloride. Copper is detected at 16.68 w%, demonstrating its successful immobilization on the functionalized zeolite surface (Fig. 7).

EDX mapping analysis of the Nano-catalyst confirms the presence and homogeneous distribution of all expected elements within the composite structure. The elemental maps demonstrate a uniform dispersion of the functional groups (APTES@TCT@S) and metal (Cu) across the zeolite surface (Fig. 8).

3.2. Efficiency of Z-NTS@CU Nano-Catalyst for synthesis of xanthene derivative

As shown in Table 5, The Z-NTS@CU Nano-catalyst demonstrated high efficiency in the one-pot synthesis of xanthene derivatives. Under mild conditions, the reactions proceeded smoothly, affording the target products in excellent yields (80–98%). This notable catalytic performance can be attributed to the synergistic contribution of its components: the zeolite provides a high-surface-area support, APTES and cyanuric chloride facilitate effective anchoring of thiosemicarbazide, and the immobilized copper functions as the active site for carbonyl activation. The catalyst also exhibited rapid reaction kinetics, completing the condensations within 20–30 min depending on the aldehyde substrate. Moreover, it is readily recoverable and reusable, retaining its activity over six consecutive cycles without significant loss of efficiency. EDX mapping confirmed uniform copper dispersion, correlating with the consistent catalytic performance observed.

As shown in Scheme 3, the synthesis of xanthene derivatives proceeds via Z-NTS@CU -catalyzed multistep condensation pathway. The catalyst activates the aldehyde carbonyl group through Lewis acid coordination, facilitating a Knoevenagel-type condensation with the enol form of dimedone to form a β-hydroxy intermediate, which subsequently undergoes dehydration to yield an α,β-unsaturated carbonyl compound. This intermediate then participates in a Michael-type addition with 2-naphthol, followed by intramolecular cyclization and final dehydration to construct the xanthene structure. Throughout the process, the copper-based catalyst enhances reaction efficiency by activating carbonyl groups, stabilizing intermediates, and promoting proton transfer, enabling high product yields under mild reaction conditions.

Table 3. N_2 adsorption-desorption isotherm data (BET)T

Catalyst	Surface area ($m^2\ g^{-1}$)	Mean pore diameter (nm)	Total pore volume ($cm^3\ g^{-1}$)
Z-PrNH$_2$	17.05	20.3	0.09
Z-NTS@Cu	6.19	16.4	0.03

Table 4. N2 adsorption-desorption isotherm data (t-plot)

Catalyst	Total specific surface area (a_1, $m^2\ g^{-1}$)	External specific surface area (a_2, $m^2\ g^{-1}$)	Micropore area (a_1- a_2, $m_2\ g^{-1}$)
Z-PrNH$_2$	10.63	0.12	10.51
Z-NTS@Cu	2.62	0.2	2.42

10.57647/ijic.2026.1702.08

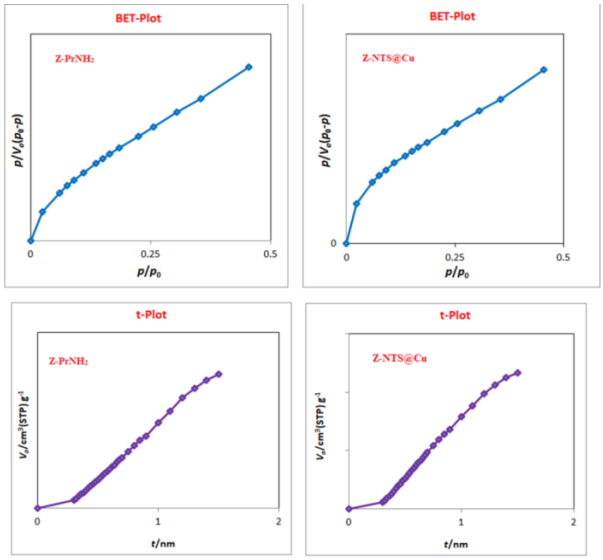

Figure 4. BET and t-plot of Z-PrNH$_2$ and Z-NTS@Cu

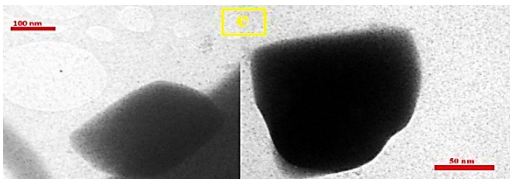

Figure 5. TEM results of Z-NTS@CU Nano-catalyst

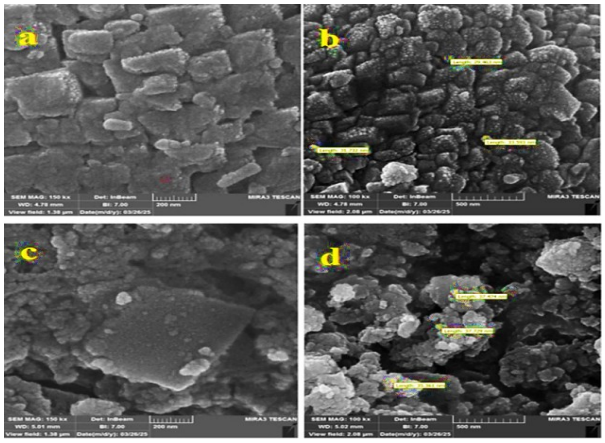

Figure 6. FE-SEM results of Z-NTS@CU Nano-catalyst

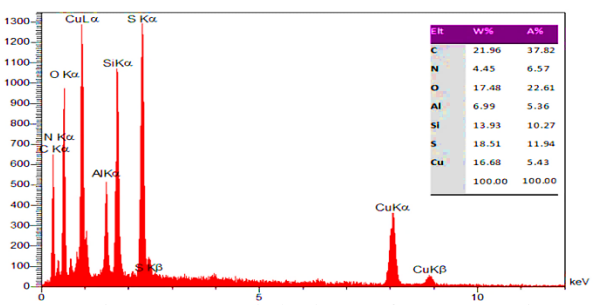

Figure 7. The EDX-EDS analysis of Z-NTS@CU Nano-catalyst

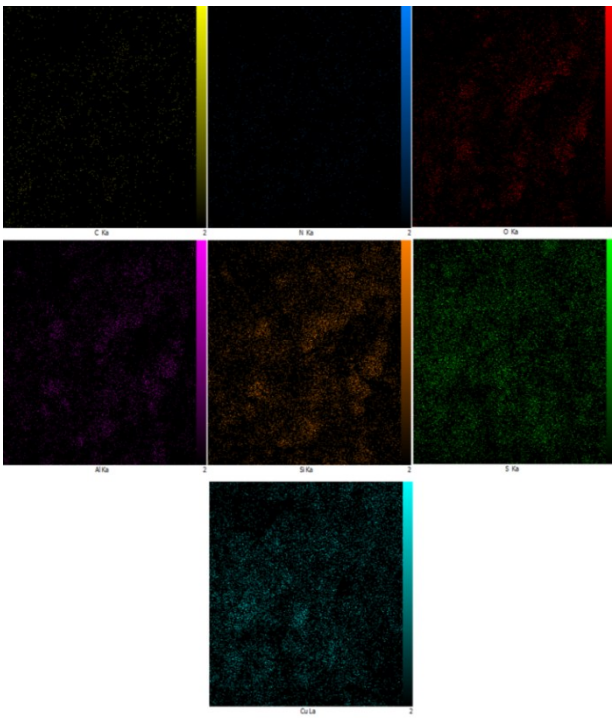

Figure 8. The EDX-Mapping analysis of Z-NTS@CU Nano-catalyst

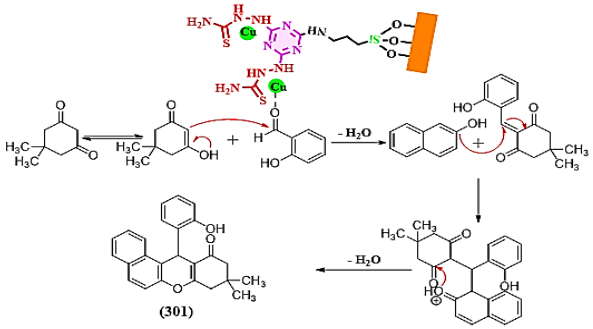

Scheme 3. Reaction mechanism for synthesis of xanthene derivatives via Z-NTS@CU-catalyzed

3.3. Spectral data for selected products

A detailed description of Spectral data for selected products can be found in the Supplementary Information (Section 2).

3.4. Comparison of the proposed method with published methods

The Z-NTS@CU nanocatalyst is highly efficient and practically applicable for the synthesis of xanthene derivatives. Under mild reaction conditions, it effectively catalyzes the condensation of benzaldehydes with dimedone and β-naphthol, affording excellent yields (85–98%) within short reaction times (20–30 min). As summarized in Table 6, this performance is comparable to or superior to several reported catalytic systems, including HPA-CDNS/NH$_2$, DABCO, (NH$_2$SO$_3$H), NH$_2$SO$_3$H, (NH$_4$)$_2$Ce(NO$_3$)$_6$, Sr(OTF)$_2$, H$_4$[Mo$_{12}$PO40], and H$_{14}$NaP$_5$W$_{30}$O$_{110}$, which often suffer from longer reaction times, limited recyclability, homogeneous reaction conditions, or complex preparation methods. The

10.57647/ijic.2026.1702.08

superior activity of the Z-NTS@CU catalyst is attributed to its high surface area, multifunctional organic anchoring sites, and immobilized copper species. this Nano-catalyst provides a robust, reusable, and environmentally benign platform that balances high catalytic efficiency, mild conditions, and excellent recyclability, making it a competitive or superior alternative for xanthene synthesis.

Table 5. Efficiency of Z-NTS@CU Nano-Catalyst for synthesis of xanthene derivative

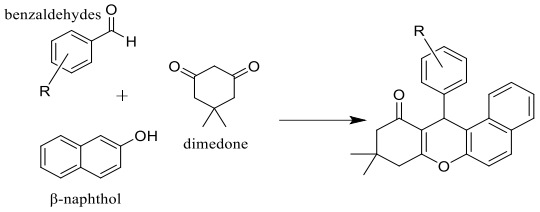

Entry	Product	Time(min)	m.p (°C)	Yield (%)
1	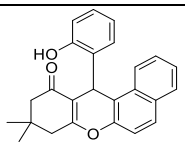	30	228-230	98
2	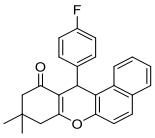	25	183-185	86
3	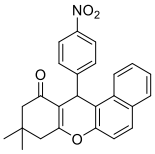	30	170-174	84
4	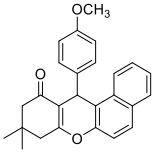	20	200-202	92
5	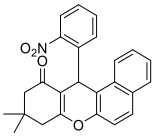	30	224-226	88
6	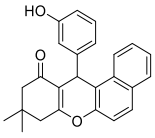	30	178-180	83
7	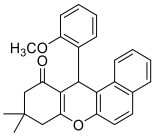	20	164-166	94
8	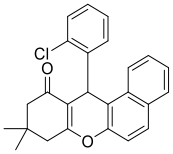	20	238-240	90
9	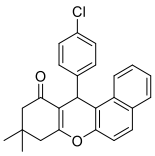	30	182-184	85

10.57647/ijic.2026.1702.08

Table 5. Efficiency of Z-NTS@CU Nano-Catalyst for synthesis of xanthene derivative (Continued)

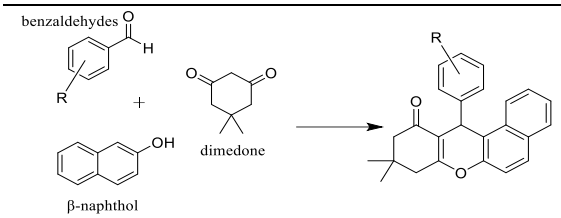

Entry	Product	Time(min)	m.p (°C)	Yield (%)
10	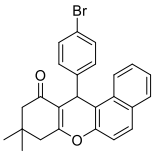	30	184-186	85
11	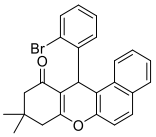	30	180-182	82
12	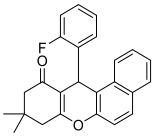	30	230 - 232	81
13	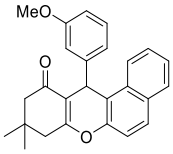	25	202-204	90
14	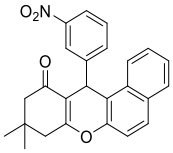	30	168-170	85
15	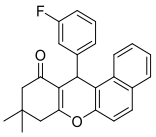	30	224-226	82
16	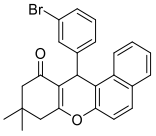	30	162-164	85
17	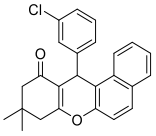	30	176-178	88
18	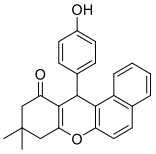	25	221-223	94
19	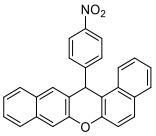	30	260-262	95
20	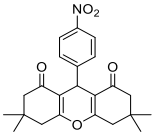	30	220-222	90

10.57647/ijic.2026.1702.08

Table 6. Comparison of the proposed method with published methods

Catalyst/System	Reaction Conditions	Yield (%)	Reaction Time	Ref.
Z-NTS@CU Nano-catalyst	Solvent-free (70 °C)	80–98	20–30 min	This work
$H_{14}NaP_5W_{30}O_{110}$[a]	Water (Reflux)	79	2 h	[42]
$H_4[Mo_{12}PO_{40}]$[b]	Water (Reflux)	81	2 h	[42]
DABCO	Water (Reflux)	60	4 h	[42]
HPA-CDNS/NH2[c]	Water (Reflux)	91	1 h	[43]
(NH_2SO_3H)[d]	Water (Reflux)	79	3 h	[42]
$(NH_4)_2Ce(NO_3)_6$[e]	DCM–ethanol (Ultrasound)	85	2 h	[44]
$Sr(OTF)_2$[f]	$ClCH_2CH_2Cl$ (80 °C)	85	5 h	[44]

a polyoxometalate, **b** phosphomolybdic acid (PMA), **c** heteropoly acid (HPA), **d** Sulfamic acid, **e** ceric ammonium nitrate (CAN), **f** strontium-trifluoromethanesulfonate

3.5. Recyclability of the Z-NTS@Cu Nano-catalyst

The Z-NTS@Cu Nano-catalyst consists of copper (Cu) nanoparticles immobilized on a zeolite nanostructured support (Z-NTS), combining the high surface area and structural stability of the support with the catalytic activity of copper. A major advantage of this catalyst is its reusability over multiple reaction cycles. Its recoverability depends on the stability of the support, the prevention of copper nanoparticle aggregation or leaching, and the retention of catalytic activity for up to six cycles (Fig.9).

The zeolite's high porosity and mechanical strength help keep the copper nanoparticles well-dispersed and stabilized, minimizing dissolution into the reaction medium. Recovery typically involves separating the catalyst by centrifugation or filtration, washing with ethanol, and drying before reuse. Studies show that Z-NTS@Cu exhibits only a slight decrease in activity after several cycles, and its efficiency remains nearly constant in many reactions. If needed, its activity can be restored through mild activation, such as brief heating or simple chemical treatment.

4. Conclusion

Herein, describe an eco-friendly and novel methodology for the synthesis of xanthene derivatives using Z-NTS@CU as a recoverable Nano-catalyst under solvent-free conditions. The newly developed heterogeneous catalyst demonstrated high efficiency across a wide range of aromatic aldehydes bearing various substituents, affording the desired products in excellent yields. The Z-NTS@Cu was characterized through various analytical techniques such as FT-IR spectroscopy, XRD patterns, TGA, BET, SEM, TEM, EDX and EDX mapping analyses. Notably, the catalyst could be reused up to six times without any significant loss of catalytic activity. Moreover, this methodology effectively overcomes common limitations such as the formation of unwanted by-products, prolonged reaction times, and the use of hazardous solvents.

Therefore, this approach is expected to have significant potential for application in organic synthesis and to represent a valuable addition to existing synthetic methodologies.

Data availability statements

All data generated or analysed during this study are included in this published article and its supplementary information files.

Supporting Information

The supporting data include products' spectral images of FTIR, 1H-NMR and 13C-NMR of products.

Acknowledgments

The authors are thankful to the Ayatollah Amoli Branch, Islamic Azad University, for the facilities provided to carry out research in chemistry research laboratory.

Funding

This work was supported by ongoing institutional funding. No additional grants to carry out or direct this particular research were obtained.

Conflict of interest

The authors declare that they have no conflicts of interest.

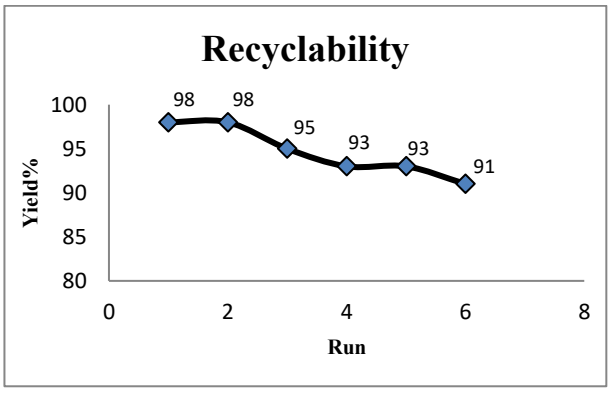

Figure 9. Recyclability chart of Z-NTS@Cu nanocatalyst

10.57647/ijic.2026.1702.08

Authors' contribution

All the authors have participated sufficiently in the intellectual content, conception, and design of this work or the analysis and interpretation of the data (when applicable), as well as the writing of the manuscript.

Availability of data and materials

The data that support the findings of this study are available from the corresponding author upon reasonable. request.

Conflict of interest

The author states that there is no conflict of interest

References

[1] Amiri MA, Younesi H, Aqmashhadi HK, Pasha GF, Asghari S, Tajbakhsh M. Efficient catalytic synthesis of xanthenes with copper immobilized on amine-modified NaY. Chem Methodol. 2024;8(1):1-22. https://doi.org/10.48309/chemm.2024.424058.1737

[2] Eissen M, Metzger JO, Schmidt E, Schneidewind U. 10 years after Rio—concepts on the contribution of chemistry to a sustainable development. Angew Chem Int Ed. 2002;41(3):414-436. https://doi.org/10.1002/1521-3773(20020201)41:3<414::AID-ANIE414>3.0.CO;2-N

[3] Beach ES, Cui Z, Anastas PT. Green chemistry: a design framework for sustainability. Energy Environ Sci. 2009;2(10):1038-1049. https://doi.org/10.1039/B904997P

[4] Mishra M, Sharma M, Dubey R, Kumari P, Ranjan V, Pandey J. Green synthesis interventions of pharmaceutical industries for sustainable development. Curr Res Green Sustain Chem. 2021;4:100174. https://doi.org/10.1016/j.crgsc.2021.100174

[5] Kurul F, Doruk B, Topkaya SN. Principles of green chemistry: building a sustainable future. Discover Chemistry. 2025;2(1):68. https://doi.org/10.1007/s44371-025-00152-9

[6] Meurig Thomas SJ. Design and applications of single-site heterogeneous catalysts: contributions to green chemistry, clean technology and sustainability. https://doi.org/10.1142/9781848169111_0001

[7] Yenare PP, Patare RD, Sonawane BP, Sanap KK. Green chemistry innovation: a systematic review on sustainable catalysis and its strategic future directions. Catal Sci Technol. 2025. https://doi.org/10.1039/D5CY00559K

[8] Yasin M, Khalid S, Yasir M, Ayub S. Advances in sustainable chemical process: catalysis, renewable, and water reduction. Indus J Biosci Res. 2025;3(1):174-184. https://doi.org/10.70749/ijbr.v3i1.479

[9] Chaltash F, Vahdat SM, Acevedo R, Ghanbari S, Qandalee M, Durán-Valle CJ, Lopez-Coca IM. Green synthesis of bis(indolyl)methane scaffolds as valuable biological materials catalyzed by Fe3O4/SiO2/PPA as a magnetic nanocatalyst. Int J Nano Dimens. 2025. https://doi.org/10.57647/ijnd-2026-1702-07

[10] Li X, Wang J, Zhang T, Yang S, Sun M, Qian X, Wang T, Zhao Y. Sustainable catalytic strategies for the transformation of plastic wastes into valued products. Chem Eng Sci. 2023;276:118729. https://doi.org/10.1016/j.ces.2023.118729

[11] Venkateswara Rao C, Tiruveedhi VB, Sudewi S, Wu HF, Pang MG, Gedda G. The role of green chemistry in achieving sustainability goals. In: Advances in Organic Waste Conversion Through Industrial Biotechnology. Cham: Springer Nature Switzerland; 2026. p. 469-494. https://doi.org/10.1007/978-3-032-11377-1_19

[12] Sultan Alqahtani A, Elbeltagi S. Advancing chemistry sustainably: from synthesis to benefits and applications of green synthesis. J Organomet Chem. 2025;1027:123508. https://doi.org/10.1016/j.jorganchem.2025.123508

[13] Lakhani P, Bhanderi D, Modi CK. Support materials impact on green synthesis and sustainable processing via heterogeneous catalysis. Discover Catal. 2024;1(1):2. https://doi.org/10.1007/s44358-024-00002-0

[14] Liang J, Liang Z, Zou R, Zhao Y. Heterogeneous catalysis in zeolites, mesoporous silica, and metal–organic frameworks. Adv Mater. 2017;29(30):1701139. https://doi.org/10.1002/adma.201701139

[15] Yu X, Williams CT. Recent advances in the applications of mesoporous silica in heterogeneous catalysis. Catal Sci Technol. 2022;12(19):5765-5794. https://doi.org/10.1039/D2CY01224D

[16] Pines H, Haag WO. Alumina: catalyst and support. I. Alumina, its intrinsic acidity and catalytic activity. J Am Chem Soc. 1960;82(10):2471-2483. https://doi.org/10.1021/ja01477a021

[17] Ndolomingo MJ, Bingwa N, Meijboom R. Review of supported metal nanoparticles: synthesis methodologies, advantages and application as catalysts. J Mater Sci. 2020;55(15):6195-6241. https://doi.org/10.1007/s10853-020-04415-x

[18] Salih AM. The purification of industrial wastewater to remove heavy metals and investigation into the use of zeolite as a remediation tool. https://doi.org/10.13140/RG.2.2.20752.76807

[19] Shamsaei E. Controllable growth of zeolitic imidazolate framework composite membranes for gas separation [doctoral dissertation]. Monash University. https://doi.org/10.4225/03/58b657b0d42c5

[20] Diab AS, Allam AA, Rudayni HA, Abukhadra MR. Zeolite-based materials for sulfate remediation: A review of structure-function insights, modification strategies, and sustainable water treatment applications. Mater Today Sustain. 2026;101308. https://doi.org/10.1016/j.mtsust.2026.101308

[21] Abinader Vasconcelos A, Len T, de Nazaré de Oliveira A, Farias da Costa AA, da Silva Souza AR, Ferreira da Costa CE, Luque R, da Rocha Filho GN, Rodrigues Noronha RC, Santos do Nascimento LA. Zeolites: A theoretical and practical approach with uses in (bio)chemical processes. Appl Sci. https://doi.org/10.3390/app13031897

[22] Zhang Q, Gao S, Yu J. Metal sites in zeolites: synthesis, characterization, and catalysis. Chem Rev. 2023;123(9):6039-6106. https://doi.org/10.1021/acs.chemrev.2c00315

[23] Wang Y, Wang C, Wang L, Wang L, Xiao FS. Zeolite fixed metal nanoparticles: New perspective in catalysis. Acc Chem Res. 2021;54(11):2579-2590. https://doi.org/10.1021/acs.accounts.1c00054

[24] Wu D, Yang M, Yu J, Dyballa M, Yang P, Li M, Hou G, Hunger M, Dai W. The role of adsorption and diffusion in improving the selectivity and reactivity of zeolite catalysts. Chem Soc Rev. 2025;54(20):9192-9244. https://doi.org/10.1039/D4CS01253F

[25] Dai J, Zhang H. Recent advances in catalytic confinement effect within micro/meso-porous crystalline materials. Small. 2021;17(22):2005334. https://doi.org/10.1002/smll.202005334

[26] Zormpa F, Treu P, Saraçi E. Advancing biomass valorization with zeolite catalysts: Focus on oxidative transformations. Sustain Chem Environ. 2025;10:100249. https://doi.org/10.1016/j.sce.2025.100249

[27] Chu D, Ma J, Liu Q, Fu J, Yin H. Effects of zeolite porosity and acidity on catalytic conversion of carbohydrates to bio-based chemicals: A review. Catal Sci Technol. 2024;14(24):6980-7001. https://doi.org/10.1039/D4CY00944F

[28] Gunda NS, Singh M, Norman L, Kaur K, Mitra SK. Optimization and characterization of biomolecule immobilization on silicon substrates using (3-aminopropyl) triethoxysilane (APTES) and glutaraldehyde linker. Appl Surf Sci. 2014;305:522-530. https://doi.org/10.1016/j.apsusc.2014.03.189

[29] Ismael BM, El-Nawawy MA, Gomaa HA, El-Gammal O. Divalent transition metal complexes of multidentate nitrogen, oxygen and sulfur containing ligand: Design, spectroscopic, theoretical molecular modeling and antioxidant like activity. Egypt J Chem. 2022;65(9):639-55. https://doi.org/10.21608/ejchem.2022.112663.5125

[30] Song Y, Gai X, Ju H, Han Z, Zhu Y, Xi D, et al. Michael-addition reaction triggering sensitive and facile detection of glutathione employing LSPR-photonic crystals. Talanta. 2026;297:128656. https://doi.org/10.1016/j.talanta.2025.128656

[31] Liu R, Fu Y, Wu F, Liu F, Zhang JJ, Yang L, et al. Modular synthesis of structurally diverse azulene-embedded polycyclic aromatic hydrocarbons by Knoevenagel-type condensation. Angew Chem Int Ed. 2023;62(21):e202219091. https://doi.org/10.1002/anie.202219091

[32] Meftah T, Zerafat MM. Nitrate removal from drinking water using organo-silane modified natural nano-zeolite. Int J Nanosci Nanotechnol. 2016;12(4):223-32. https://doi.org/10.7508/ijnnt.2016.04.003

[33] Barquist KN. Synthesis and environmental adsorption applications of functionalized zeolites and iron oxide/zeolite composites [dissertation]. Iowa (IA): The University of Iowa; 2009. https://doi.org/10.17077/etd.9aa8vru4

[34] Taghartapeh MR, Pesyan NN, Rashidnejad H, Khavasi HR, Soltani A. Synthesis, spectroscopic and photophysical studies of xanthene derivatives. J Mol Struct. 2017;1149:862-73. https://doi.org/10.1016/j.molstruc.2017.08.053

[35] Mileski TC. Aplicação de corantes benzazólicos fluorescentes por ESIPT para a revelação de manchas de sangue em cenas de crime e a síntese do luminol. https://doi.org/10.25358/openscience-1143

[36] Ghashghaei R, Ghassamipour S. A green procedure for synthesis of xanthene derivatives: Micellar solution of sodium dodecylphosphonate catalyzes condensation reaction of aldehydes and β-naphthol in aqueous media. 2014. https://doi.org/10.13140/RG.2.2.27538.89289

[37] Pirouzmand M, Gharehbaba AM, Ghasemi Z. Synthesis of xanthene derivatives using template-containing Zn/MCM-41 as a green and reusable catalyst: Effect of the template. J Mex Chem Soc. 2016;60(4):183-7. https://doi.org/10.29356/jmcs.v60i4.122

[38] Sadjadi S. Efficient synthesis of xanthene derivatives in aqueous media in the presence of Cu-anchored furfural imine-functionalized halloysite. https://doi.org/10.13140/RG.2.2.22868.81284

[39] Sadjadi S, Heravi MM, Daraie M. Cyclodextrin nanosponges: A potential catalyst and catalyst support for synthesis of xanthenes. Res Chem Intermed. 2017;43(2):843-57. https://doi.org/10.1007/s11164-016-2687-8

[40] Sudha S, Pasha MA. Ultrasound assisted synthesis of tetrahydrobenzo[c]xanthene-11-ones using CAN as catalyst. Ultrason Sonochem. 2012;19(5):994-998. https://doi.org/10.1016/j.ultsonch.2012.01.001

[41] Li J, Tang W, Lu L, Su W. Strontium triflate catalyzed one-pot condensation of β-naphthol, aldehydes and cyclic 1,3-dicarbonyl compounds. Tetrahedron Lett. 2008;49(50):7117-7120. https://doi.org/10.1016/j.tetlet.2008.10.046

[42] Alizadeh MH, Kermani T, Tayebee R. A method for the acetylation of alcohols catalyzed by heteropolyoxometallates. Monatsh Chem. 2007;138(2):165-170. https://doi.org/10.1007/s00706-006-0573-2

[43] Sadjadi S, Abedian-Dehaghani N, Heydari A, Heravi MM. Chitosan bead containing metal–organic framework encapsulated heteropolyacid as an efficient catalyst for cascade condensation reaction. Sci Rep. 2023;13(1):2797. https://doi.org/10.1038/s41598-023-29548-2

[44] Kumar S, Dubey S, Saxena N, Awasthi SK. (NH4)2Ce(NO3)6 as an inexpensive, eco-friendly, efficient catalyst for the synthesis of 5-substituted 1H-tetrazoles from nitriles. Tetrahedron Lett. 2014;55(44):6034-6038. https://doi.org/10.1016/j.tetlet.2014.09.010

Appendix

Supporting Information

1. Characterization

Fourier transforms infrared spectroscopy (FT-IR)

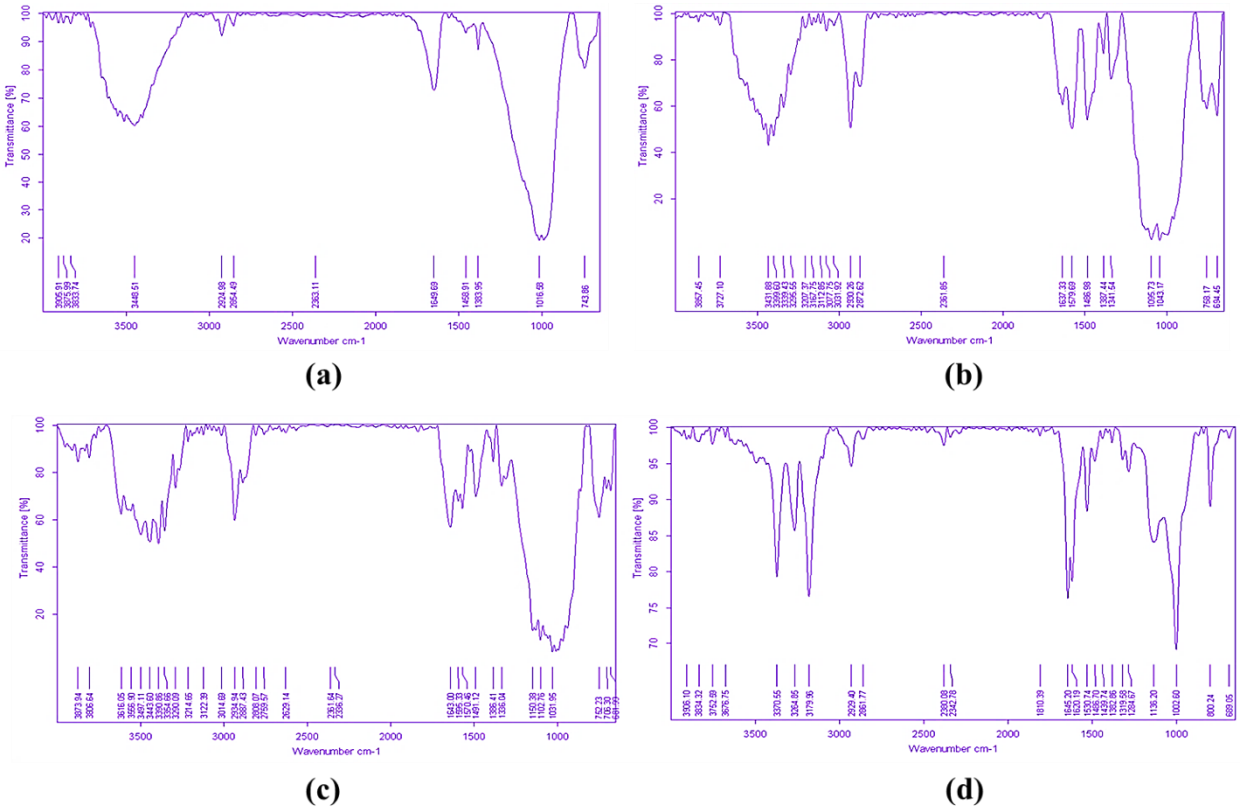

Figure S.1. FT-IR spectrum of (a) Zeolite Nano-particle (b) Z-PrNH$_2$ Nano-composite (c) Z-NT Nano-composite (d) Z-NTS Nano-composite

Table S.1. BJH, Langmuir and t-plot analyses of Z-NTS@CU Nano-composite

	Langmuir plot
Vm	2.9213[cm^3(STP) g^{-1}]
as,Lang	12.715[m^2 g^{-1}]
B	0.3308

	t plot
Plot data	Adsorption branch
a_1	6.6266[m^2 g^{-1}]
V_1	0[cm^3 g^{-1}]

	BJH plot
Plot data	Adsorption branch
V_p	0.089998[cm^3 g^{-1}]
$r_{p,peak}$(Area)	1.22[nm]
a_p	23.989[m^2 g^{-1}]

10.57647/ijic.2026.1702.08

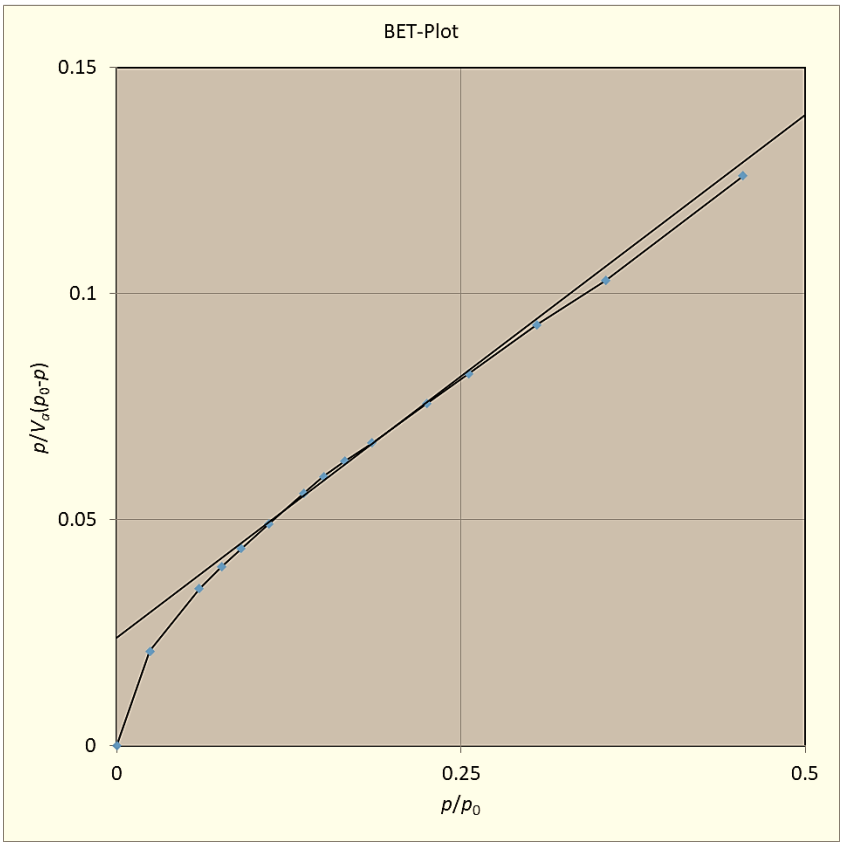

Figure S.2. The BET plot of Z-NTS Nano-composite

Table S.2. Xanthene derivatives were synthesized in the presence of Z-NTS@CU Nano-catalyst

entry	Product	entry	Product	entry	Product
1	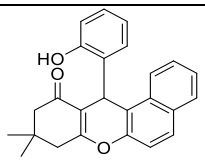	8	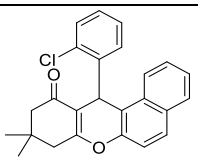	15	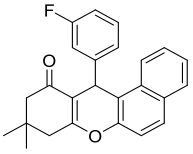
2	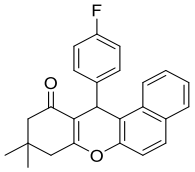	9	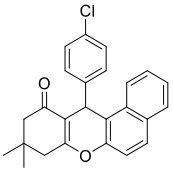	16	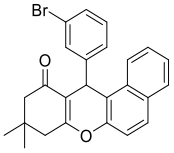
3	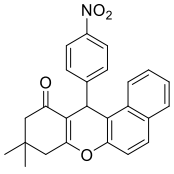	10	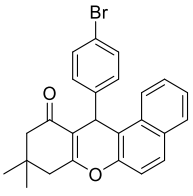	17	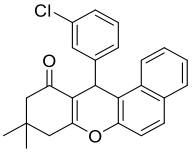
4	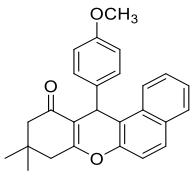	11	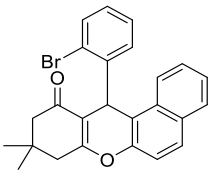	18	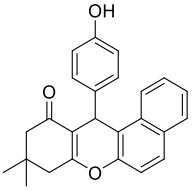

Table S.2. Xanthene derivatives were synthesized in the presence of Z-NTS@CU Nano-catalyst (Continued)

entry	Product	entry	Product	entry	Product
5	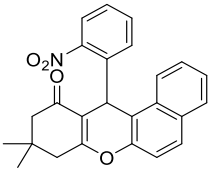	12	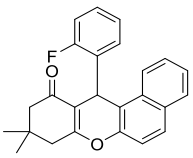	19	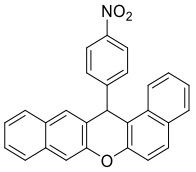
6	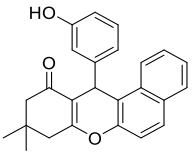	13	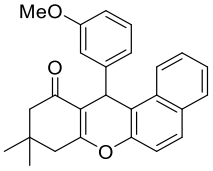	20	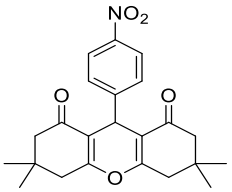
7	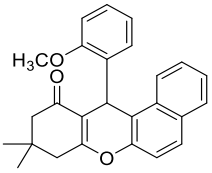	14	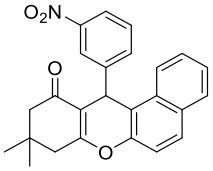		

2. Spectral data for selected products

12-(2-hydroxyphenyl)-9,9-dimethyl-8,9,10,12-tetrahydro-11H-benzo[a]xanthen-11-one (1)

^{1}H NMR (400MHz, DMSO- d_6): 0.94 (s, 3H, CH_3), 1.08 (s, 3H, CH_3), 2.08-2.11 (d, 1H, CH_2), 2.32-2.36 (d, 1H, CH_2), 2.50-2.60 (m, 1H, CH_2), 2.69-2.73 (d, 1H, CH_2), 5.75 (s, 1H, CH), 6.59-6.62 (t, 1H, Ar-H), 6.69-6.71 (d, 1H, Ar-H), 6.85-6.89 (m, 1H, Ar-H), 7.00-7.02 (d, 1H, Ar-H), 7.38-7.43 (m, 2H, Ar-H), 7.46-7.50 (m, 1H, Ar-H), 7.48-7.89 (t, 2H, Ar-H), 8.31-8.33 (d, 1H, Ar-H), 9.66 (s, 1H, -OH); ^{13}C NMR (100 MHz, DMSO-d_6): δ 158.8, 154.0, 151.8, 144.8, 134.5, 133.1, 130.0, 128.7, 127.7, 127.3, 126.0, 125.5, 123.6, 121.9, 120.3, 118.6, 117.9, 113.3, 81.9, 51.0, 46.1, 38.5, 36.8, 33.5, 29.7, 28.0, 26.9, 24.9, 21.0.

12-(4-fluorophenyl)-9,9-dimethyl-8,9,10,12-tetrahydro-11H-benzo[a]xanthen-11-one (2)

^{1}H NMR (400MHz, DMSO- d_6): 0.94 (m, 3H, CH_3), 1.12 (s, 3H, CH_3), 2.17-2.21 (d, 1H, CH_2), 2.37-2.42 (m, 1H, CH_2), 2.62-2.67 (d, 1H, CH_2), 2.74-2.78 (d, 1H, CH_2), 5.65 (s, 1H, CH), 7.05-7.09 (t, 2H, Ar-H), 7.35-7.39 (m, 2H, Ar-H), 7.47-7.57 (m, 3H, Ar-H), 7.97-8.00 (m, 2H, Ar-H), 8.07-8.09 (d, 1H, Ar-H); ^{13}C NMR (100 MHz, DMSO-d6): δ 196.6, 164.4, 159.1, 158.7, 138.5, 137.0, 135.9, 132.7, 127.7, 127.1, 126.9, 125.5, 121.6, 115.7, 114.9, 113.5, 113.5, 81.7, 51.6, 42.7, 35.2, 27.6, 26.5, 21.0.

12-(4-Methoxyphenyl)-9,9-dimethyl-8,9,10,12-tetrahydro-11H-benzo[a]xanthen-11-one (4)

^{1}H NMR (400MHz, DMSO- d_6): 0.89 (s, 3H, CH_3), 1.06 (s, 3H, CH_3), 2.11-2.15 (d, 1H, CH_2), 2.32-2.36 (d, 1H, CH_2), 2.56-2.60 (d, 1H, CH_2), 2.67-2.71 (d, 1H, CH_2), 3.63 (s, 3H, O-CH_3), 5.51 (s, 1H, CH), 6.73-6.75 (d, 2H, Ar-H), 7.18-7.20 (d, 1H, Ar-H), 7.41-7.51 (m, 3H, Ar-H), 7.89-7.92 (d, 2H, Ar-H), 8.02-8.04 (d, 1H, Ar-H); ^{13}C NMR (100 MHz, DMSO-d_6): δ 195.9 (C=O), 164.1, 157.3, 152.3, 151.8, 149.9, 145.7, 138.4, 132.9, 129.8, 128.4, 127.6, 126.4, 125.2, 124.3, 121.7, 114.3, 113.6, 112.9, 55.3 (OCH_3), 51.8, 41.9, 34.7, 31.3, 29.7, 27.3.

12-(2-Nitrophenyl)-9,9-dimethyl-8,9,10,12-tetrahydro-11H-benzo[a]xanthen-11-one (5)

^{1}H NMR (400MHz, DMSO- d_6): 0.76 (s, 3H, CH_3), 1.04 (s, 3H, CH_3), 2.03-2.07 (d, 1H, CH_2), 2.28-2.32 (d, 1H, CH_2), 2.56 (s, 1H, CH_2), 2.68-2.72 (m, 1H, CH_2), 6.36 (s, 1H, CH), 7.02-7.04 (d, 1H, Ar-H), 7.31-7.35 (m, 1H, Ar-H), 7.43-7.52 (m, 4H, Ar-H), 7.87-7.89 (d, 1H, Ar-H), 7.95-7.97 (d, 1H, Ar-H), 8.01-8.03 (d, 1H, Ar-H), 8.43-8.45 (d, 1H, Ar-H); ^{13}C NMR (100 MHz, DMSO-d_6): δ 196.0, 164.4, 153.1, 149.6, 147.8, 145.2, 138.9, 134.3, 132.1, 130.5, 129.2, 127.9, 126.8, 125.4, 123.9, 121.6, 118.4, 114.9, 82.1, 51.6, 42.3, 34.9, 31.5, 29.8, 27.5.

10.57647/ijic.2026.1702.08

NMR spectrum of selected products

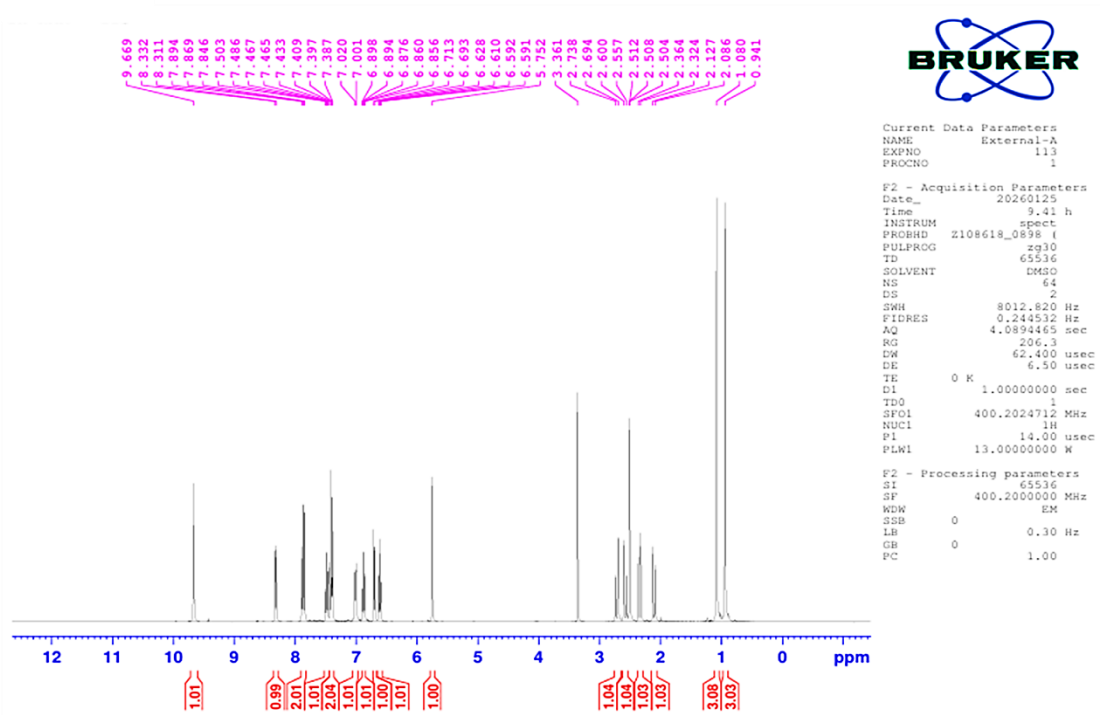

Figure S.3. [1]H NMR spectrum of the product 12-(2-hydroxyphenyl)-9,9-dimethyl-8,9,10,12-tetrahydro-11H-benzo[a]xanthen-11-one (1)

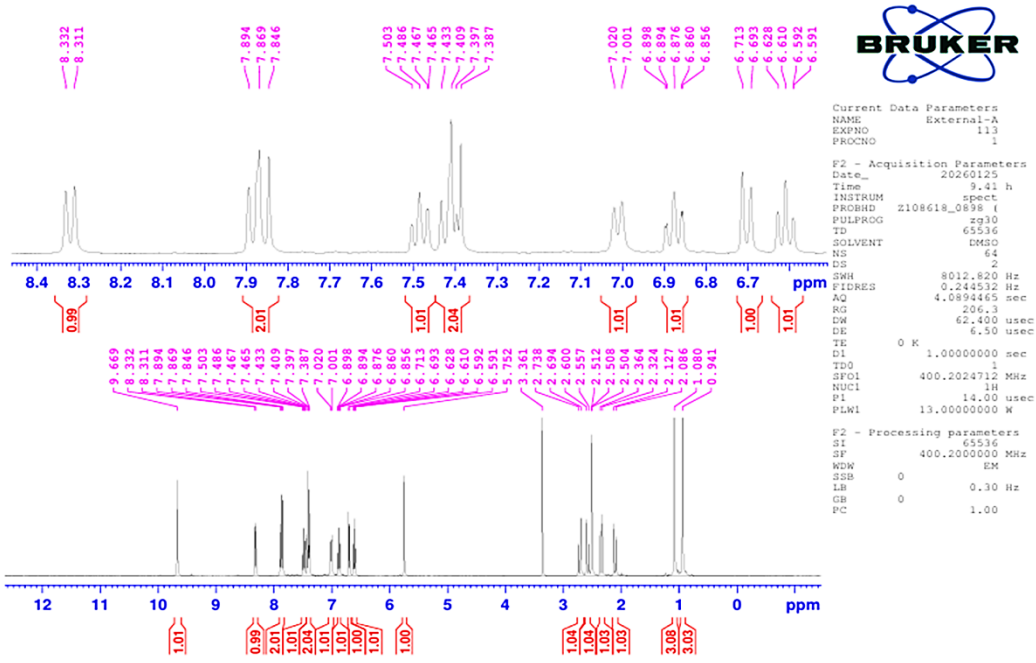

Figure S.4. Expanded [1]H NMR spectrum of the product 12-(2-hydroxyphenyl)-9,9-dimethyl-8,9,10,12-tetrahydro-11H-benzo[a]xanthen-11-one (1)

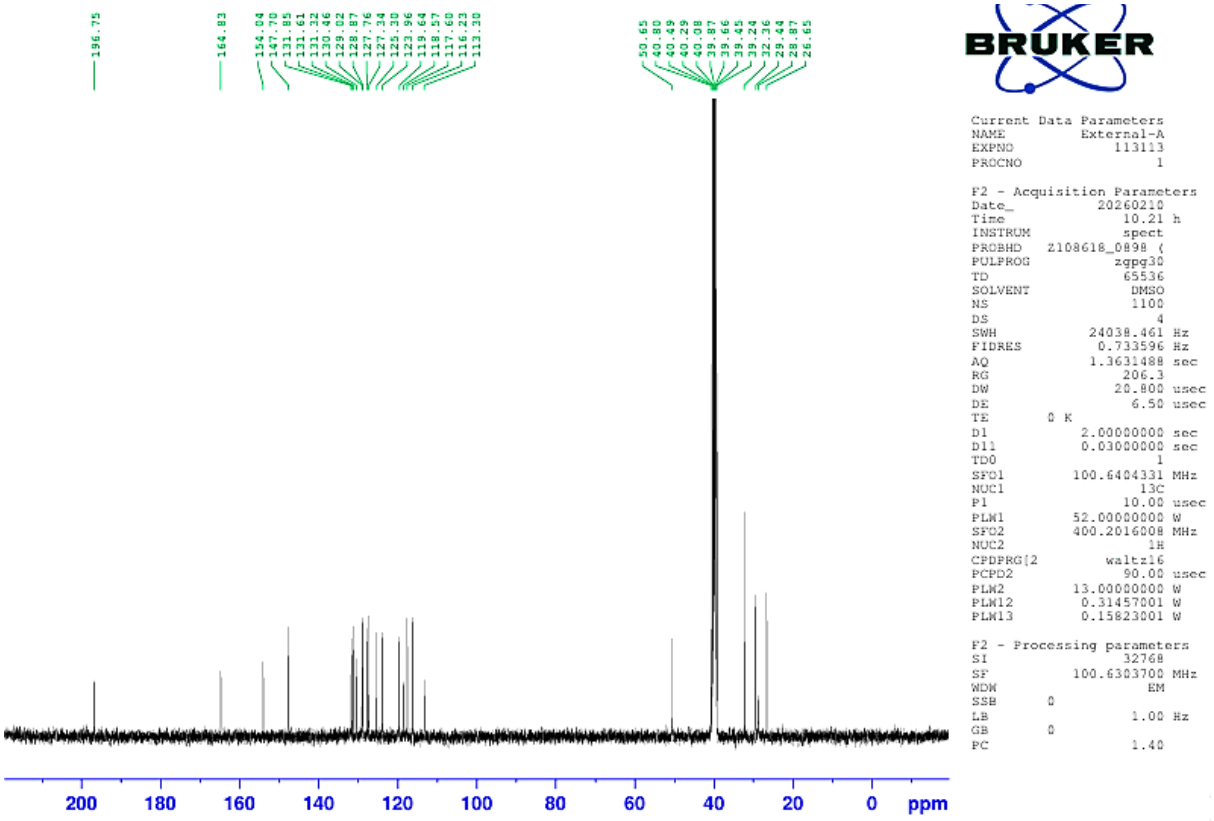

Figure S.5. ^{13}C NMR spectrum of the product 12-(2-hydroxyphenyl)-9,9-dimethyl-8,9,10,12-tetrahydro-11H-benzo[a]xanthen-11-one (1)

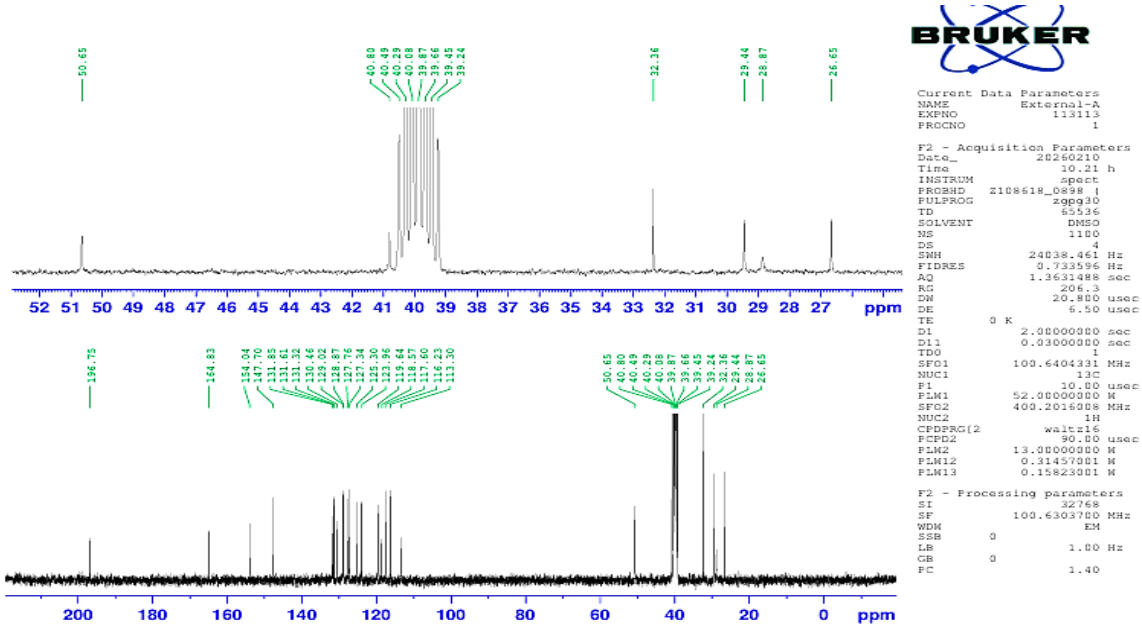

Figure S.6. Expanded ^{13}C NMR spectrum of the product 12-(2-hydroxyphenyl)-9,9-dimethyl-8,9,10,12-tetrahydro-11H-benzo[a]xanthen-11-one (1)

10.57647/ijic.2026.1702.08

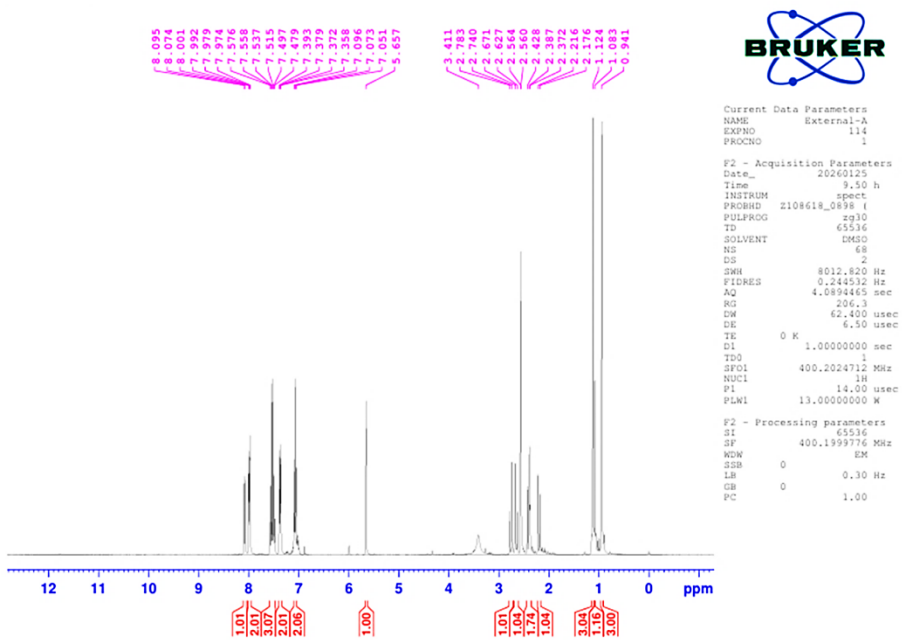

Figure S.7. [1]H NMR spectrum of the product 12-(4-fluorophenyl)-9,9-dimethyl-8,9,10,12-tetrahydro-11H-benzo[a]xanthen-11-one (2)

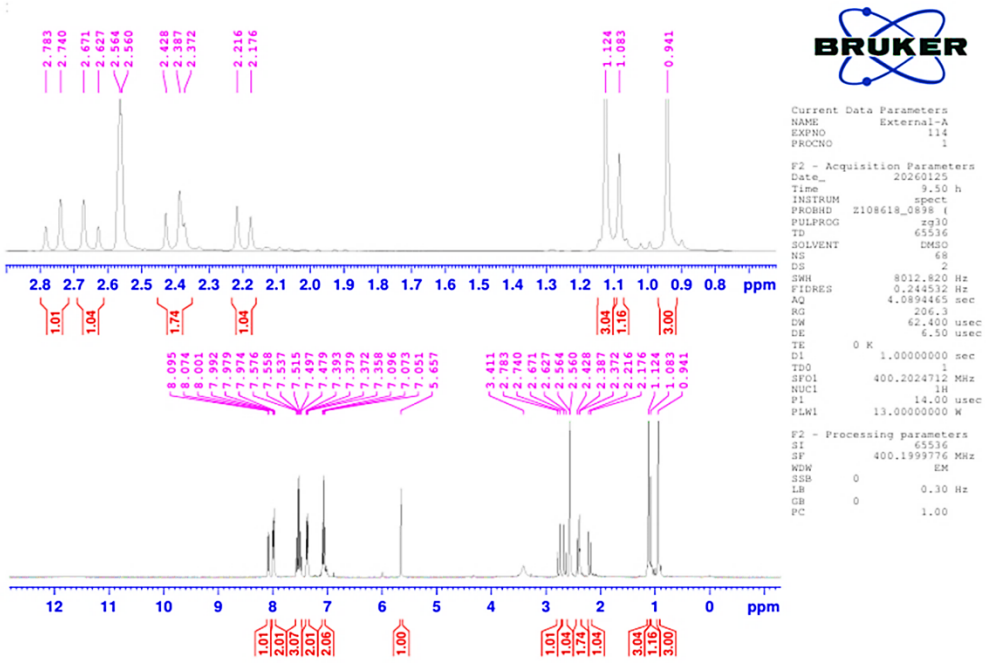

Figure S.8. Expanded [1]H NMR spectrum of the product 12-(4-fluorophenyl)-9,9-dimethyl-8,9,10,12-tetrahydro-11H-benzo[a]xanthen-11-one (2)

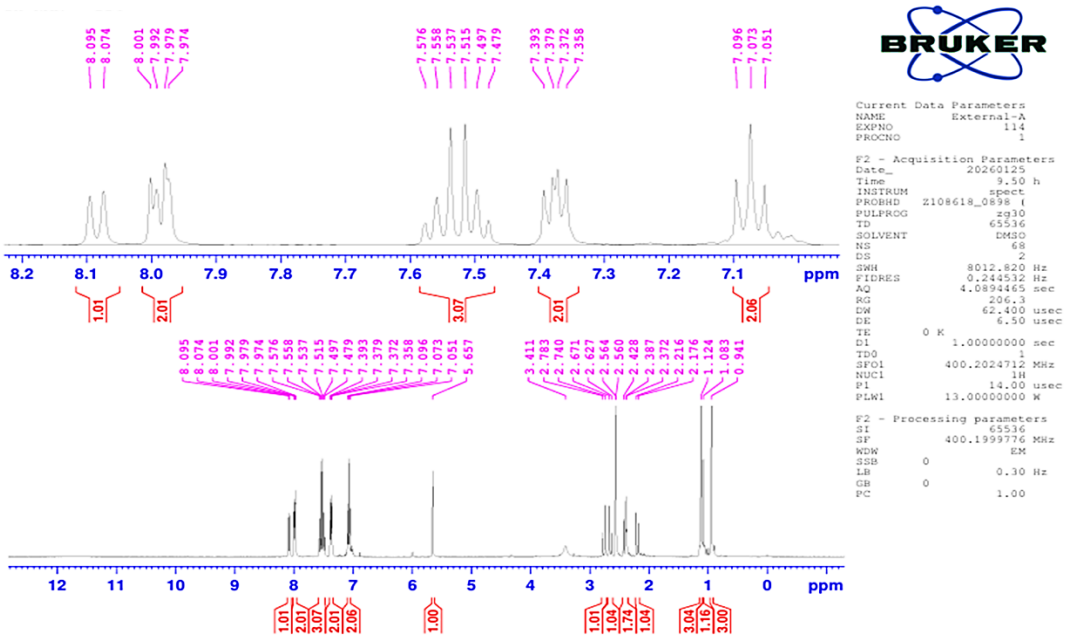

Figure S.9. Expanded [1]H NMR spectrum of the product 12-(4-fluorophenyl)-9,9-dimethyl-8,9,10,12-tetrahydro-11H-benzo[a]xanthen-11-one (2)

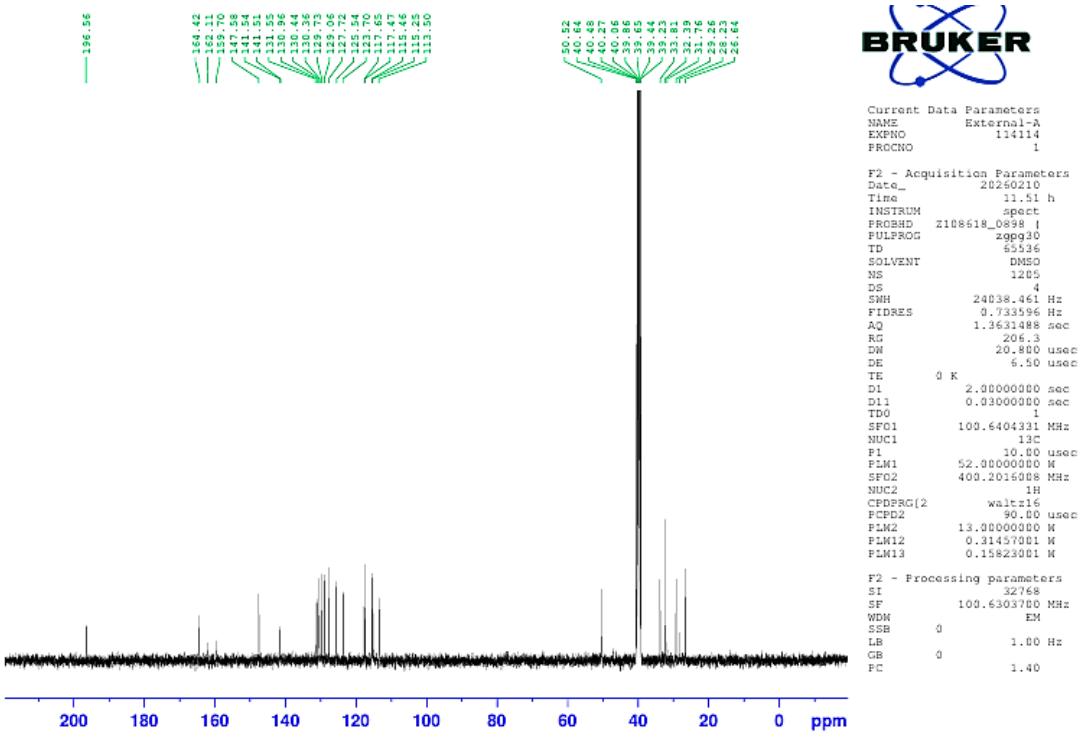

Figure S.10.[13]C NMR spectrum of the product 12-(4-fluorophenyl)-9,9-dimethyl-8,9,10,12-tetrahydro-11H-benzo[a]xanthen-11-one (2)

10.57647/ijic.2026.1702.08

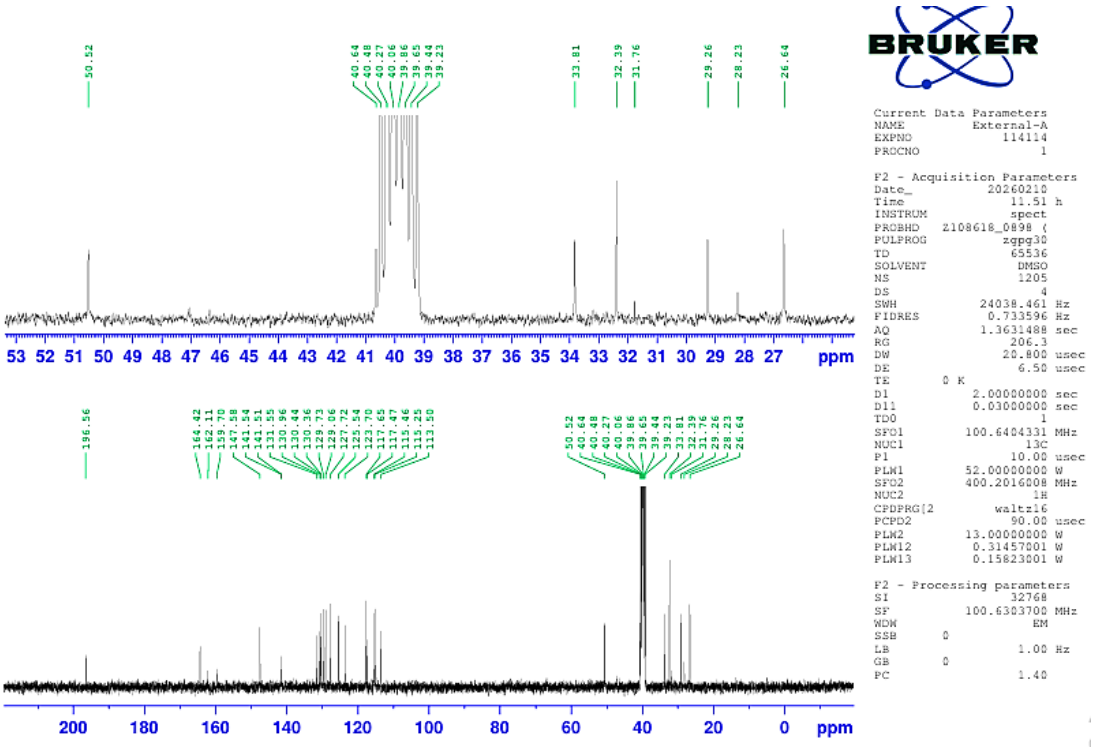

Figure S.11. Expanded ^{13}C NMR spectrum of the product 12-(4-fluorophenyl)-9,9-dimethyl-8,9,10,12-tetrahydro-11H-benzo[a]xanthen-11-one (2)

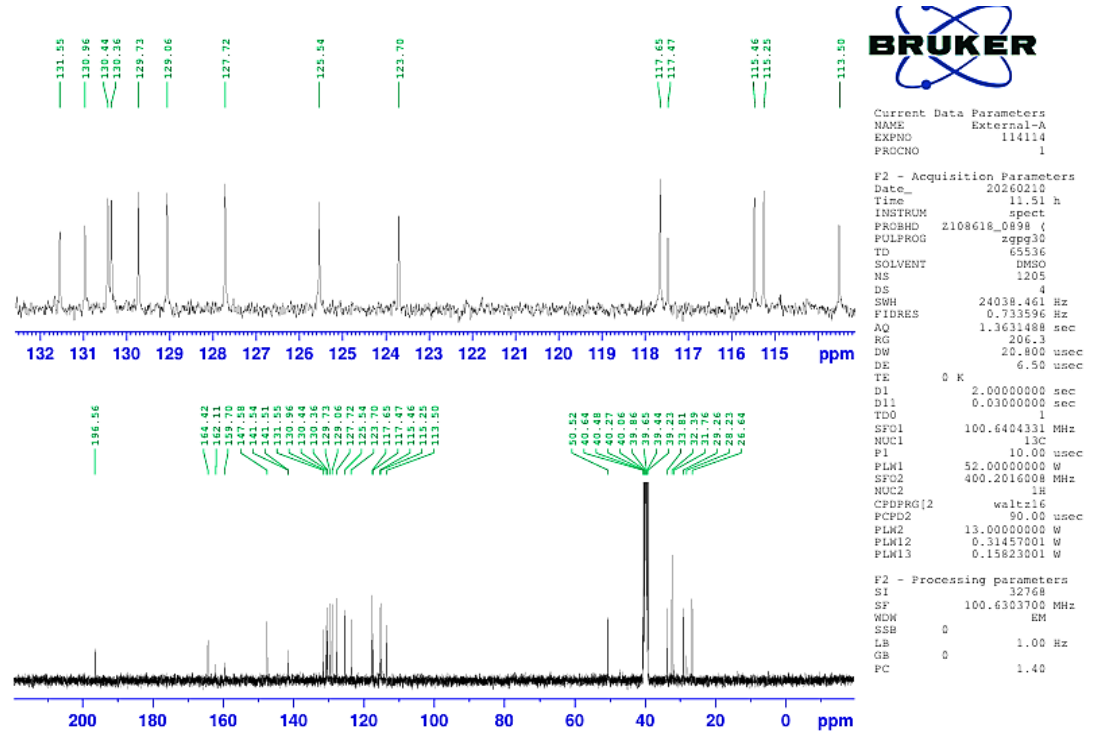

Figure S.12. Expanded ^{13}C NMR spectrum of the product 12-(4-fluorophenyl)-9,9-dimethyl-8,9,10,12-tetrahydro-11H-benzo[a]xanthen-11-one (2)

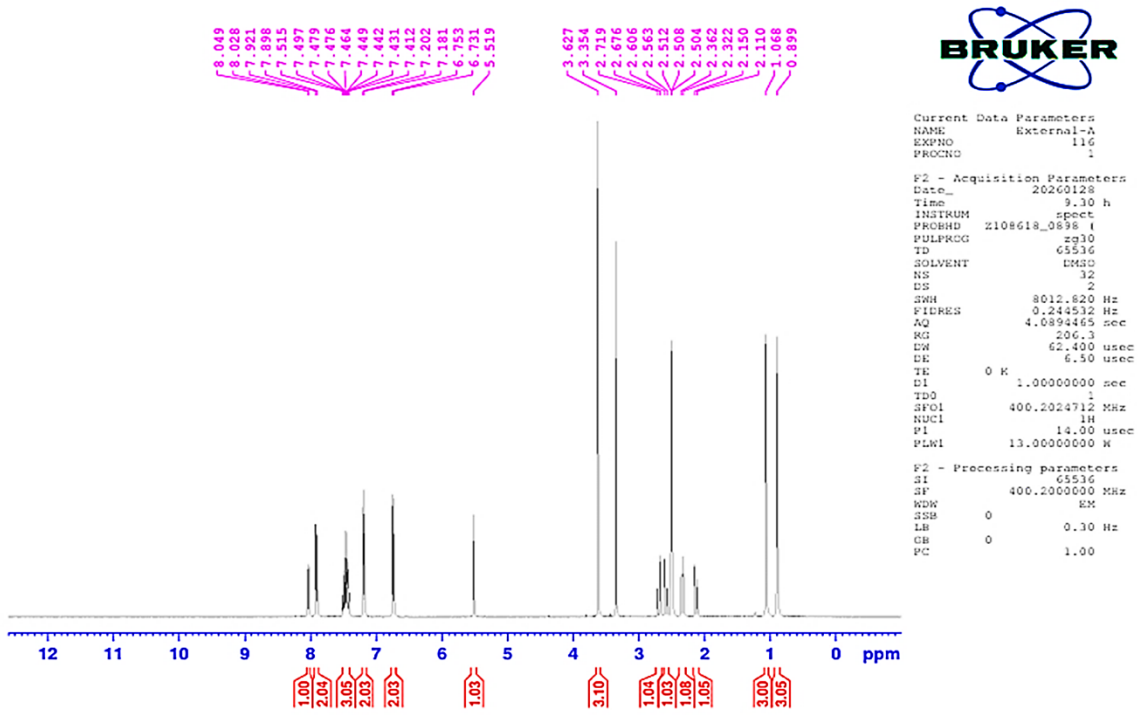

Figure S.13. [1]H NMR spectrum of the product 12-(4-Methoxyphenyl)-9,9-dimethyl-8,9,10,12-tetrahydro-11H-benzo[a]xanthen-11-one (4)

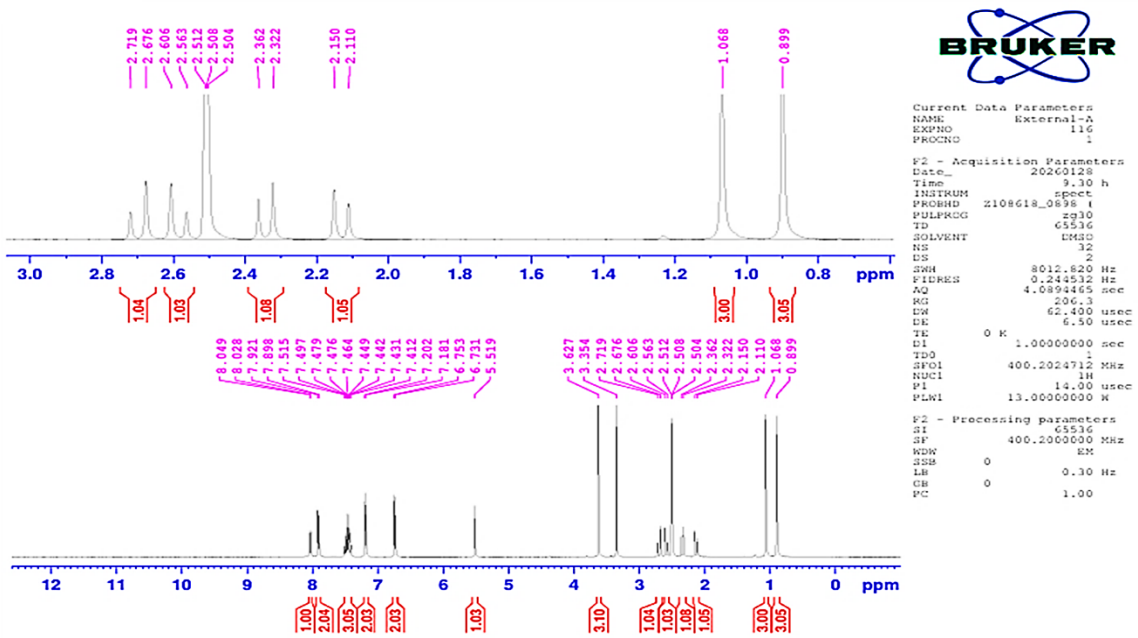

Figure S.14. Expanded [1]H NMR spectrum of the product 12-(4-Methoxyphenyl)-9,9-dimethyl-8,9,10,12-tetrahydro-11H-benzo[a]xanthen-11-one (4)

10.57647/ijic.2026.1702.08

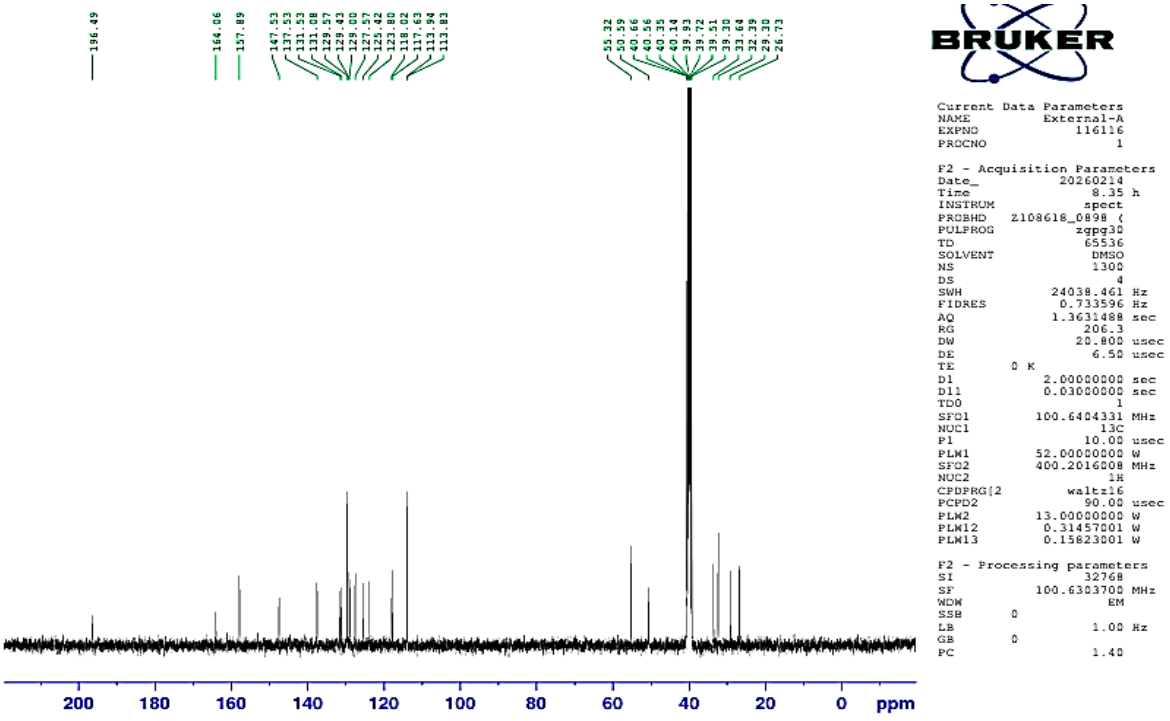

Figure S.15. ^{13}C NMR spectrum of the product 12-(4-Methoxyphenyl)-9,9-dimethyl-8,9,10,12-tetrahydro-11H-benzo[a]xanthen-11-one (4)

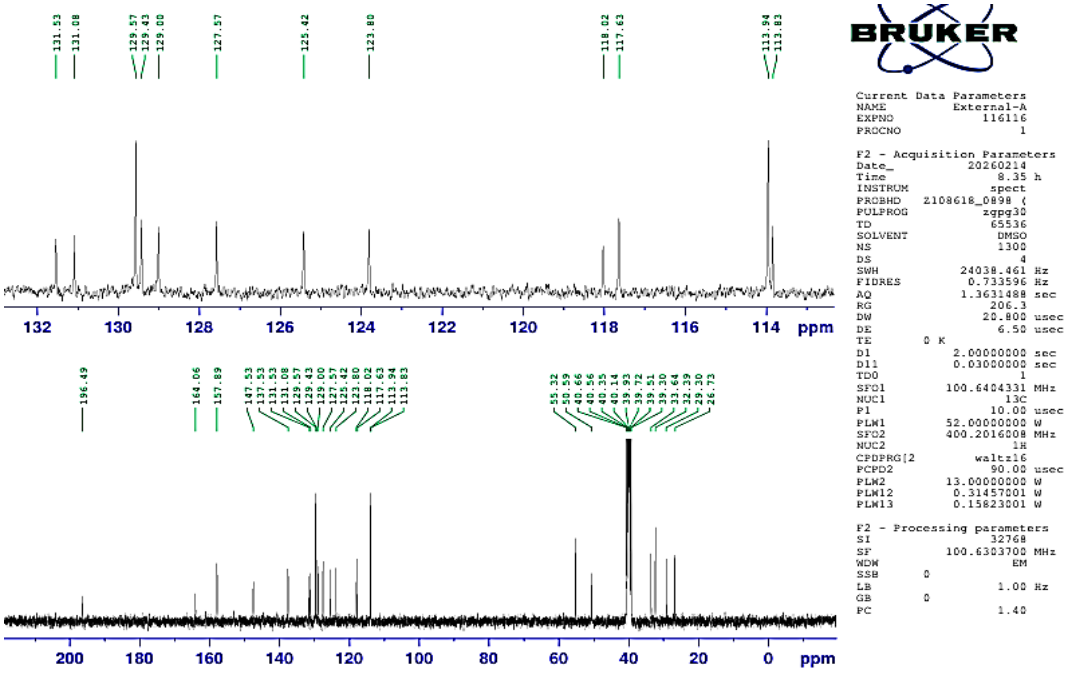

Figure S.16. Expanded ^{13}C NMR spectrum of the product 12-(4-Methoxyphenyl)-9,9-dimethyl-8,9,10,12-tetrahydro-11H-benzo[a]xanthen-11-one (4)

10.57647/ijic.2026.1702.08

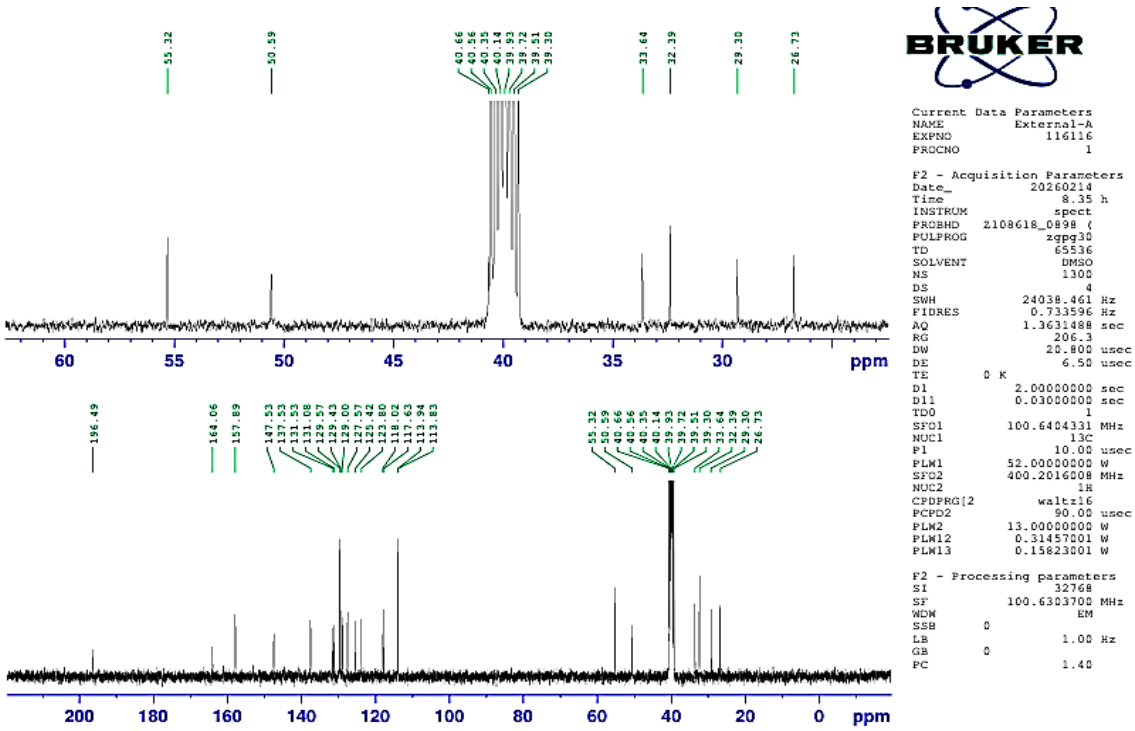

Figure S.17. Expanded ^{13}C NMR spectrum of the product 12-(4-Methoxyphenyl)-9,9-dimethyl-8,9,10,12-tetrahydro-11H-benzo[a]xanthen-11-one (4)

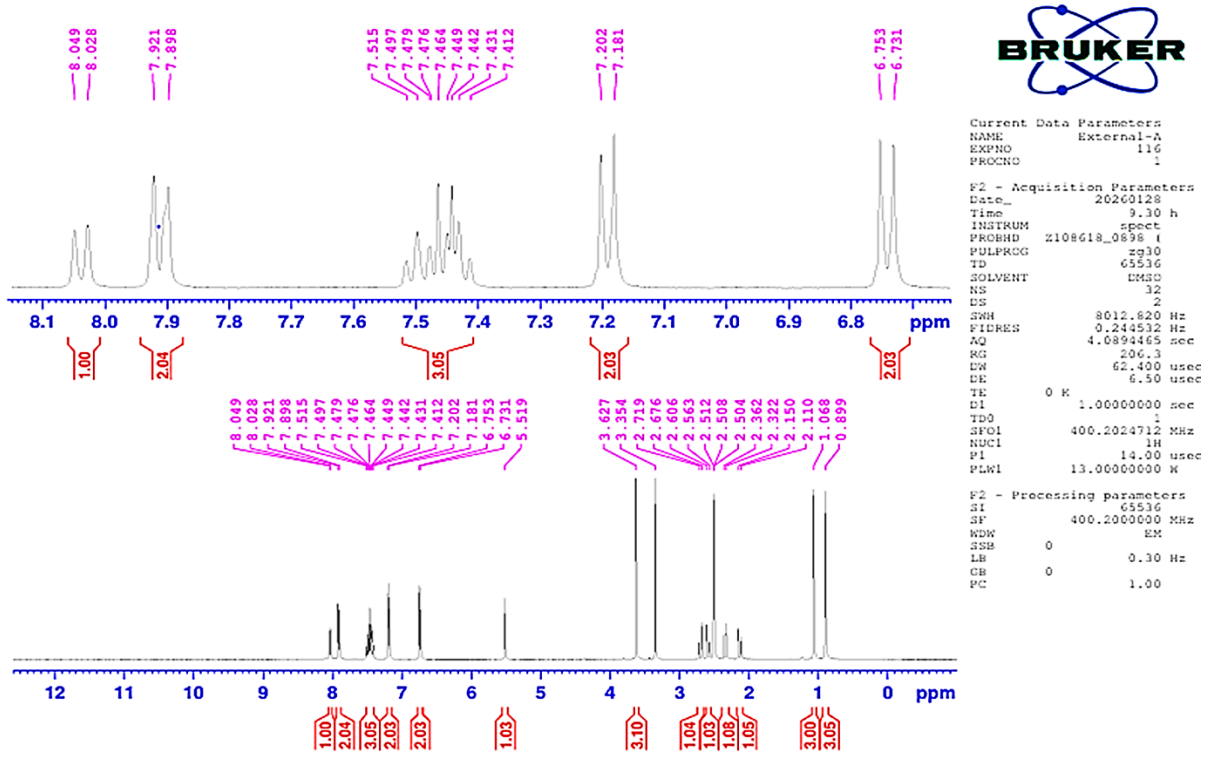

Figure S.18. Expanded ^{1}H NMR spectrum of the product 12-(4-Methoxyphenyl)-9,9-dimethyl-8,9,10,12-tetrahydro-11H-benzo[a]xanthen-11-one (4)

10.57647/ijic.2026.1702.08

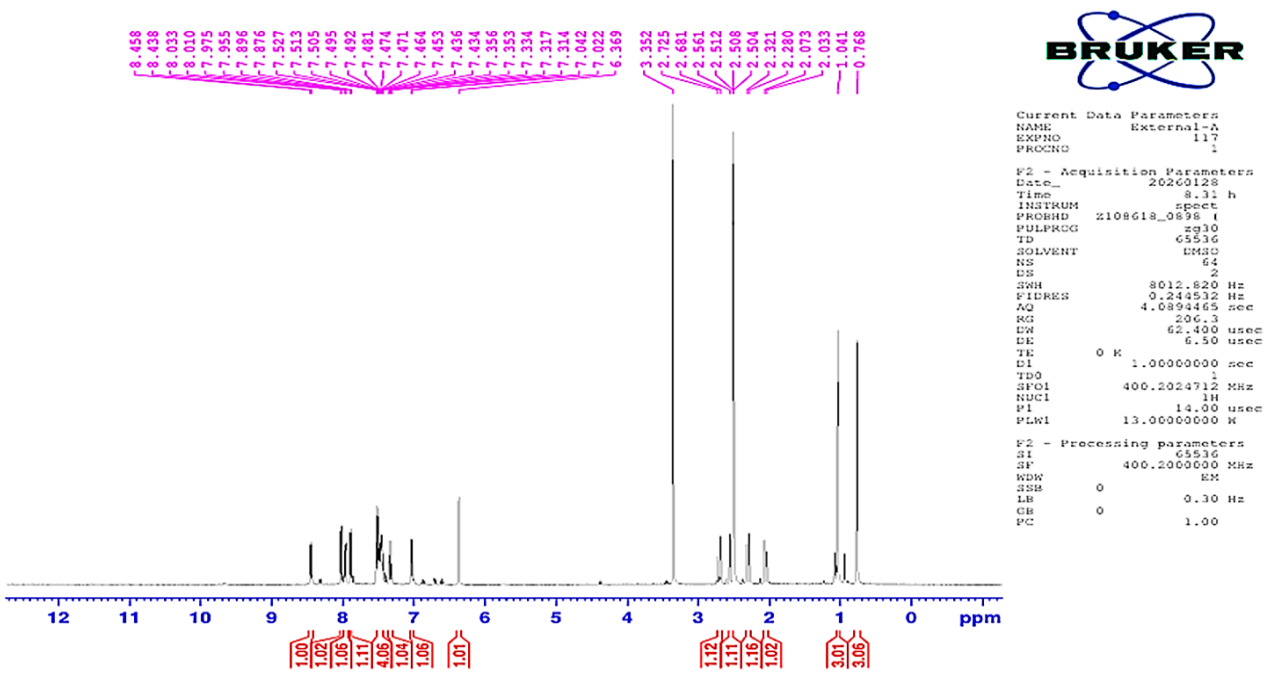

Figure S.19. [1]H NMR spectrum of the product 12-(2-Nitrophenyl)-9,9-dimethyl-8,9,10,12-tetrahydro-11H-benzo[a]xanthen-11-one (5)

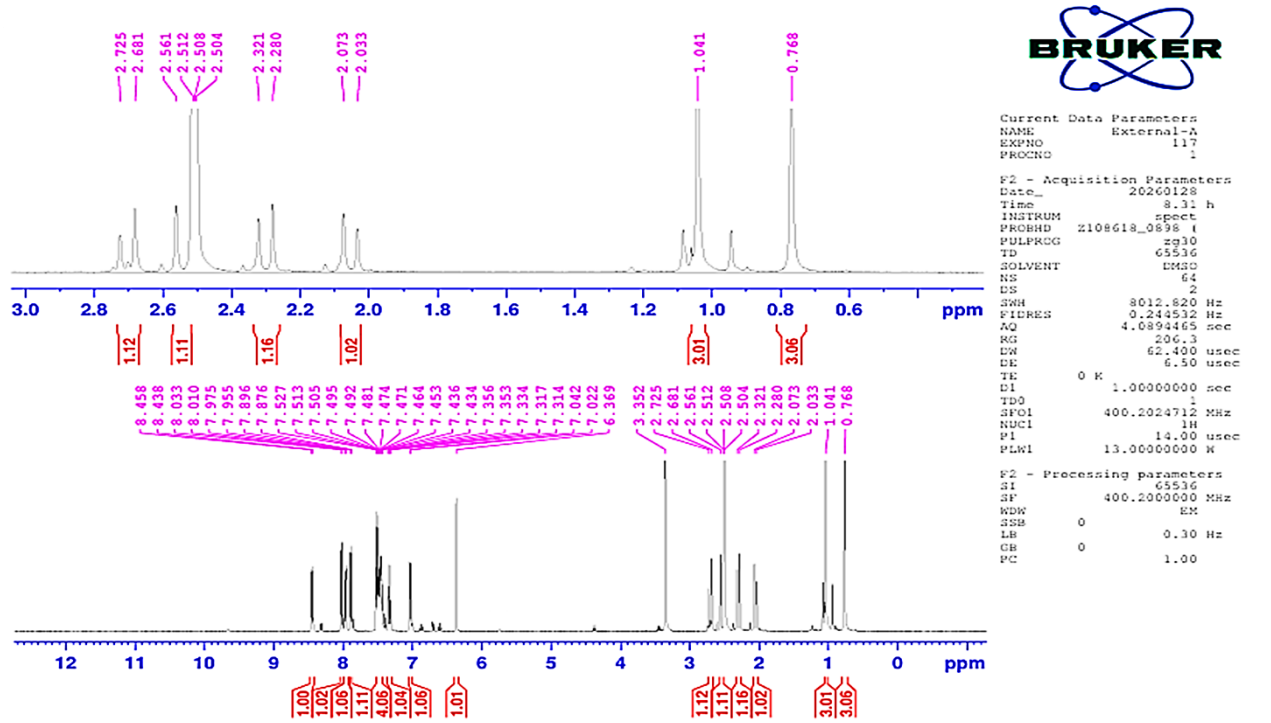

Figure S.20. Expanded [1]H NMR spectrum of the product 12-(2-Nitrophenyl)-9,9-dimethyl-8,9,10,12-tetrahydro-11H-benzo[a]xanthen-11-one (5)

10.57647/ijic.2026.1702.08

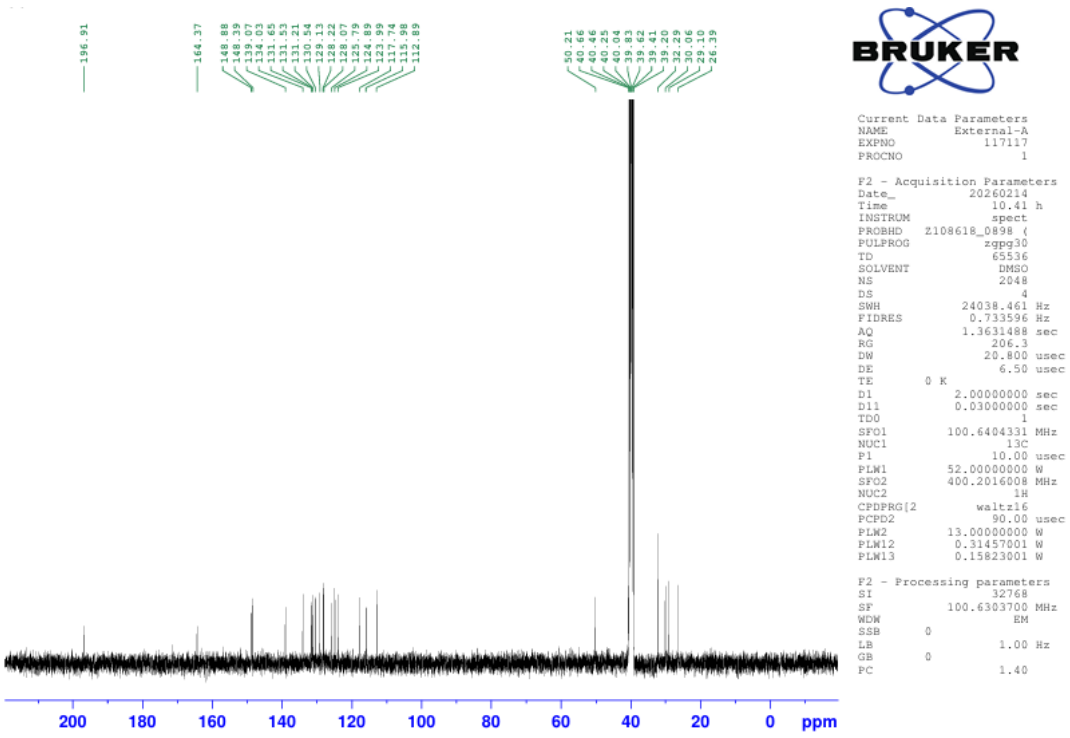

Figure S.21. ^{13}C NMR spectrum of the product 12-(2-Nitrophenyl)-9,9-dimethyl-8,9,10,12-tetrahydro-11H-benzo[a]xanthen-11-one (5)

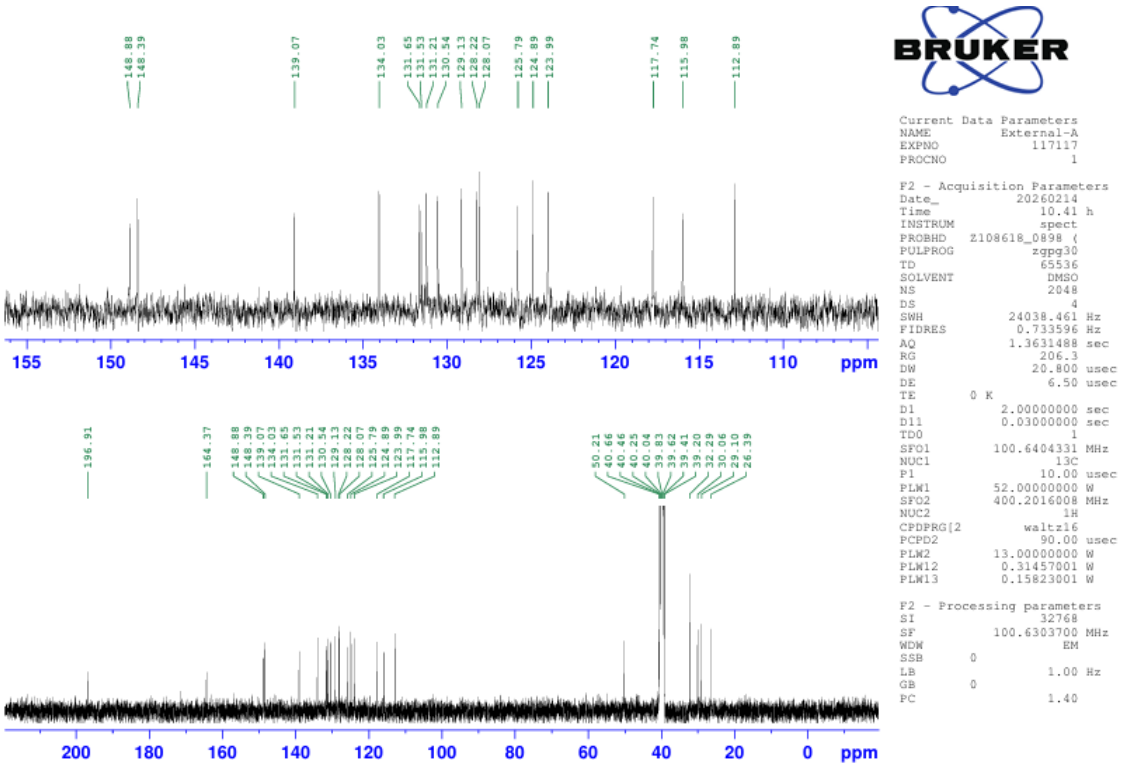

Figure S.22. Expanded ^{13}C NMR spectrum of the product 12-(2-Nitrophenyl)-9,9-dimethyl-8,9,10,12-tetrahydro-11H-benzo[a]xanthen-11-one (5)

10.57647/ijic.2026.1702.08

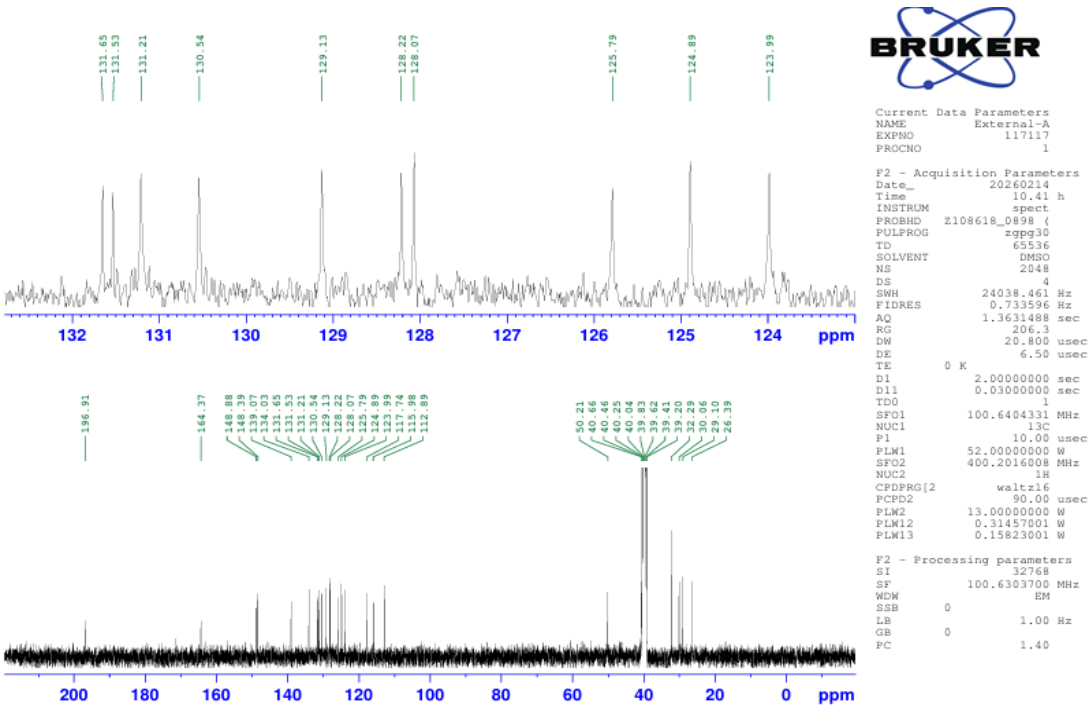

Figure S.23. Expanded ^{13}C NMR spectrum of the product 12-(2-Nitrophenyl)-9,9-dimethyl-8,9,10,12-tetrahydro-11H-benzo[a]xanthen-11-one (5)

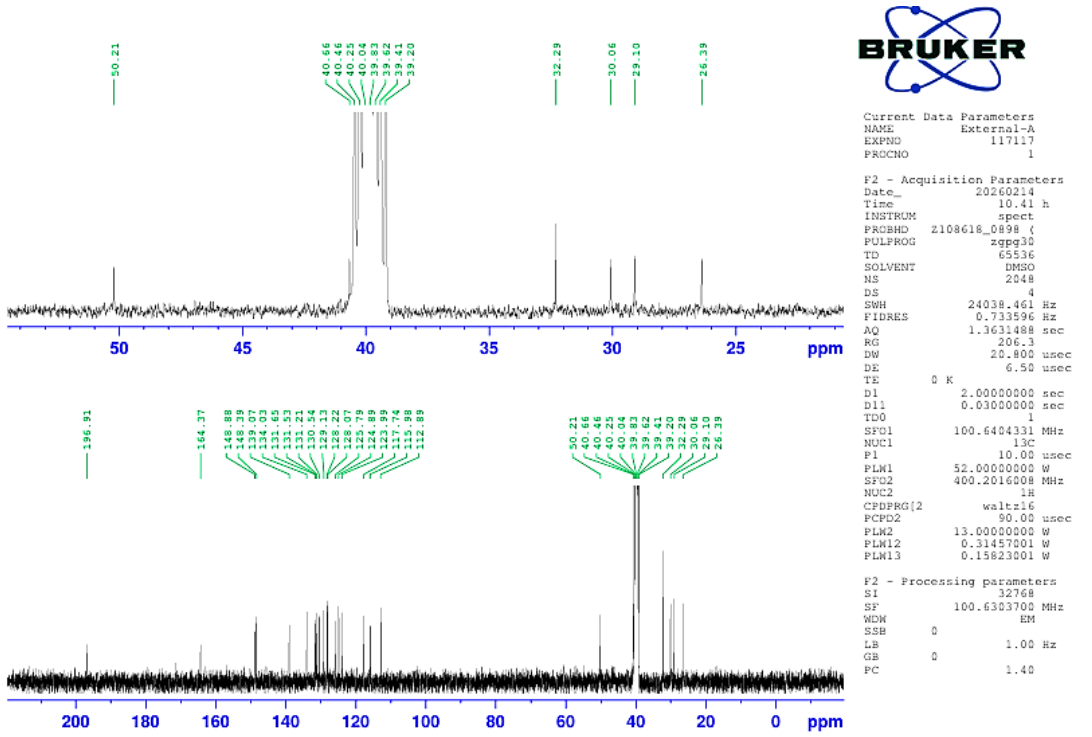

Figure S.24. Expanded ^{13}C NMR spectrum of the product 12-(2-Nitrophenyl)-9,9-dimethyl-8,9,10,12-tetrahydro-11H-benzo[a]xanthen-11-one (5)